UNIVERSITY OF CALIFORNIA,
IRVINE

Ex Vivo Corneal Electromechanical Reshaping

THESIS

submitted in partial satisfaction of the requirements
for the degree of

MASTER OF SCIENCE

in Biomedical Engineering

by

Aditya Prajval Kumar

Thesis Committee:
Professor Brian Wong, Chair (UC Irvine)
Professor Zhongping Chen (UC Irvine)
Professor Michael Hill (Occidental College)

2023

DEDICATION

To

my parents

for their unwavering support in my time of need

and their infinite love

TABLE OF CONTENTS

	Page
LIST OF FIGURES	v
LIST OF TABLES	vi
ACKNOWLEDGEMENTS	vii
ABSTRACT OF THE THESIS	viii
INTRODUCTION	1
CHAPTER 1: STATEMENT OF PURPOSE AND AIMS	3
CHAPTER 2: BACKGROUND	6
Physiology and Structure of the Eye	6
Current Electrochemical Therapies	12
Electrochemistry	19
Optical Coherence Tomography (OCT)	21
Second Harmonic Generation (SHG)	25
CHAPTER 3: RESEARCH DESIGN AND METHODS	29
Experimental Setup	29
Methods of Studying Curvature Change	31
Methods of Studying Collagen Orientation Change	37
CHAPTER 4: RESULTS	39
Curvature Data	39
Collagen Orientation Data	41
CHAPTER 5: DISCUSSION	44
Summary of OCT Findings	44
OCT Limitations	44
Summary of SHG Findings	45

SHG Limitations 46
Overall Limitations 46

CHAPTER 6: CONCLUSION 48

REFERENCES 49

APPENDIX A: MATLAB SCRIPT 53

APPENDIX B: SWEPT-SOURCE OCT BUILD 62

LIST OF FIGURES

		Page
Figure 1	3-Electrode Setup	29
Figure 2	Fabrication of Lens	30
Figure 3	Flow Chart of Curvature Code	32
Figure 4	2D Cross-Sectional Line Fitting	33
Figure 5	MATLAB 3D Filtering Code	34
Figure 6	Fitted Sphere Example	35
Figure 7	Calibration of System	36
Figure 8	Fitted Sphere for Cornea	39
Figure 9	Scatter Plot of Pre- vs. Post- EMR Curvature	41
Figure 10	SHG Orientation Graph	42
Figure 11	SHG of Cornea	43

LIST OF TABLES

		Page
Table 1	Curvature Values Before and After EMR	40
Table 2	SHG Kolmogorov-Smirnov Results	42

ACKNOWLEDGEMENTS

I would like to express my sincere gratitude to several individuals who have played a crucial role in the successful completion of my master's thesis.

First and foremost, I extend my heartfelt thanks to Katelyn Dilley for her invaluable support in helping me become a part of this lab. Her guidance was instrumental in acquainting me with the lab's environment and the intricacies of previous work on electromechanical reshaping of the cornea. Above all, I would like to thank her for her friendship.

I am immensely grateful to Dr. Brian Wong for his role as my Principal Investigator throughout this project. His expertise, guidance, and continuous encouragement have been pivotal in shaping the direction of my research and fostering my academic growth.

I would like to extend my appreciation to Theodore Nguyen and Clara Chao for their unwavering assistance during the experiments. Their willingness to share their knowledge and lend a helping hand significantly contributed to the smooth execution of the project.

I am indebted to Dr. Mike Hill of Occidental College for his invaluable contributions to the electrochemistry aspect of my research. His insights and expertise greatly enhanced the depth and quality of my work.

I am thankful to Dr. Zhongping Chen’s lab for generously allowing me to utilize their OCT system. Their collaboration and support were instrumental in acquiring the necessary data for my study.

I would also like to express my gratitude to Daniel Kim for his significant contribution in helping me refine my thesis. His insights and feedback played a crucial role in shaping the clarity and coherence of my work.

Research reported in this thesis was supported by the Office Of The Director, National Institutes Of Health of the National Institutes of Health under Award Number S10OD028698. The content is solely the responsibility of the authors and does not necessarily represent the official views of the National Institutes of Health.

Lastly, I would like to acknowledge FIJI for providing the software that played a pivotal role in the analysis of my results. The availability of this tool greatly facilitated the processing and interpretation of my data.

Each of these individuals has made an indelible mark on my academic journey, and I am truly honored to have had the privilege to work alongside them. Their contributions have been invaluable, and I am thankful for the unwavering support they provided throughout this endeavor.

ABSTRACT OF THE THESIS

Ex Vivo Corneal Electromechanical Reshaping

by

Aditya Prajval Kumar

Master of Science in Biomedical Engineering

University of California, Irvine, 2023

Professor Brian Wong

The transparent outer layer of the eye, known as the cornea, has a vital function in bending and directing light onto the retina, which is essential for achieving clear vision. Current methods of correcting refractive errors that are becoming increasingly popular include LASIK and PRK surgeries; however, these invasive techniques come with downsides as well such as permanent thinning of the cornea. This thesis proposes the use of a non-invasive technique called electromechanical reshaping (EMR) that can be applied to the cornea to induce curvature change. EMR was performed on New Zealand white rabbit globes using a concave platinum lens as the working electrode in a 3-electrode setup. The primary outcomes to be measured include the aforementioned curvature change of the cornea and the change in distribution of collagen orientation: to observe such changes the advanced imaging modalities of optical coherence tomography (OCT) and second harmonic generation (SHG) have been employed. The curvature data can be analyzed through a developed MATLAB approach that reconstructs the 3D surface of the cornea from 2D cross-sectional OCT images and sphere-fits the surface to extract the radius of curvature. The collagen structural change can be analyzed in FIJI software using OrientationJ

to quantify the orientation of collagen fibers. These methods serve as a sound quantitative way to analyze the outcomes of EMR. This thesis found that the mean curvature increased from 5193.73 μm ± 597.09 μm to 5429.16 μm ± 736.08 μm following EMR application. Regarding collagen structural change, most of the eyes did not show a statistically significant difference following EMR application. Due to experimental error because of the lack of standardization of pressure, however, the corneal curvature did not consistently increase and the corneas did not resemble the radius of curvature of the platinum lens used in EMR (7.486 mm). Future directions include standardization of the pressure applied on the cornea by the platinum lens, simultaneous OCT imaging during EMR application, seeing if corneas post-EMR retain curvature changes, and transitioning to applying EMR on eyes intact in New Zealand white rabbit heads.

INTRODUCTION

The cornea, which is the transparent outermost layer of the eye, plays a crucial role in refracting light and focusing it onto the retina, enabling clear vision. Corneal reshaping techniques have garnered considerable attention in the field of ophthalmology, offering potential solutions for various visual impairments and refractive errors. In particular, the ability to modify corneal curvature without surgical intervention has opened up new avenues for non-invasive vision correction. Non-invasive methods offer advantages in terms of reduced risks, faster recovery, and potential reversibility.

Electromechanical reshaping (EMR) is a technique that remodels collagen-rich tissues by applying an electric potential to electrolyze water, creating a proton gradient within the collagenous tissue. This proton gradient alters the chemical properties of the extracellular matrix of the tissues and allows the tissues to respond to mechanical remodeling. EMR has first been used to remodel cartilage and skin tissues, and in recent years, this technique has been applied to corneal reshaping as well; in a previous study, EMR has been successfully applied to alter the focal length of *ex vivo* rabbit cornea. EMR allows for precise and localized modifications, which will hopefully establish it as a viable candidate for non-invasive vision correction. Further investigating the effectiveness and safety of EMR in *ex vivo* rabbit eye models will serve as a stepping stone towards clinical translation [1]–[3].

Optical Coherence Tomography (OCT) has emerged as a valuable imaging modality for non-invasive, high-resolution assessment of corneal morphology. By utilizing low-coherence interferometry, OCT provides cross-sectional images that reveal detailed information about the cornea's structure. In this thesis, OCT will be employed to visualize the curvature changes induced by EMR in ex vivo rabbit eyes [4].

Collagen, the main structural component of the cornea, plays a critical role in maintaining its shape and integrity. **Second Harmonic Generation (SHG)** microscopy has proven to be a powerful imaging technique for visualizing collagen fibers within tissues. SHG selectively detects nonlinear optical signals, providing insights into the microstructural changes occurring in the cornea during reshaping procedures. This thesis will utilize SHG microscopy to investigate potential collagen structural change resulting from EMR [5].

The primary objective of this thesis is to investigate the application of EMR in *ex vivo* rabbit eyes, with a focus on curvature change assessment through OCT and collagen structure evaluation through SHG. The thesis aims to quantify EMR-induced curvature changes and investigate potential alterations in collagen structure following EMR.

The experimental design entails using freshly enucleated rabbit eyes and applying a specialized electrode for controlled EMR on the cornea. Curvature changes will be evaluated using OCT through 2D cross-sectional imaging, MATLAB-based 3D reconstruction, and sphere-fitting for the radius of curvature. SHG corneal images will be analyzed through FIJI software to evaluate collagen structural changes, enabling quantifiable analysis of the effectiveness of EMR for corneal application.

By shedding light on the safety and efficacy of electrode-induced corneal reshaping and employing advanced imaging modalities to assess both curvature changes and potential collagen damage, this thesis aims to provide valuable insights that can inform the development of this non-surgical approach for vision correction. The findings from this study may lead to improved EMR outcomes.

CHAPTER 1: STATEMENT OF PURPOSE AND AIMS

The findings of this research have significant implications for the field of non-invasive vision correction. By investigating the application of corneal EMR in *ex vivo* rabbit eyes, this thesis contributes to the development of an alternative method for correcting refractive errors. If the results demonstrate the safety and efficacy of this technique, it may pave the way for the future clinical translation of electrode-based corneal reshaping procedures. Such advancements have the potential to offer patients with a non-surgical option that is non-invasive, carries reduced risks, and allows for faster recovery compared to traditional approaches.

One of the primary concerns when introducing corneal EMR is ensuring patient safety. The utilization of second harmonic generation (SHG) microscopy allows for a comprehensive evaluation of collagen structural change. Assessing the safety profile of electrode-induced corneal reshaping through this imaging technique enables a better understanding of the potential risks and side effects associated with the treatment.

The findings of this thesis on the underlying mechanisms of corneal EMR and its quantitative effects on corneal curvature and collagen structure contribute to the understanding of how the cornea responds to EMR. These insights may open avenues for development of more targeted and personalized approaches. This tailored strategy holds promise for clinical implementation, enabling controlled curvature changes to correct refractive errors.

To ensure the effectiveness, safety, and clinical viability of electromechanically reshaping the cornea, it is crucial to adopt a systematic approach in its evaluation and implementation.

Systematic corneal reshaping research involves meticulous data collection and analysis techniques. This entails utilizing advanced imaging modalities such as optical

coherence tomography (OCT) and second harmonic generation (SHG) microscopy to obtain accurate and comprehensive measurements of corneal curvature changes and collagen structural change. These imaging techniques can quantify the extent of corneal curvature modification and assess potential collagen structural change at a microstructural level, respectively. In addition, this requires the usage of appropriate statistical methods for data analysis that allows for the identification of significant trends, correlations, and potential confounding factors. Systematic data collection and analysis enhance the reliability of the thesis outcomes.

Adopting a systematic approach in corneal reshaping research necessitates the development of a standardized experimental design. This includes defining OCT parameters, confocal microscope settings and imaging depth for SHG, consistent loading of samples for imaging, and potentiostat parameters. By adhering to a well-defined experimental protocol, the research outcomes are reproducible and comparable.

Moreover, systematic corneal reshaping research focuses on selecting appropriate outcome measures. Selecting relevant outcome measures, such as changes in corneal curvature and collagen fiber organization, ensures that the research outcomes capture the key aspects of corneal reshaping and provide meaningful insights.

Ultimately, this systematic approach contributes to the development of an effective and evidence-based non-invasive vision correction technique.

The central question driving this thesis is whether the cornea can be reshaped from EMR, with the changes in corneal curvature measured before and after the procedure using optical coherence tomography (OCT). This question stems from the potential of non-invasive vision correction techniques that offer an alternative option to surgical interventions such as LASIK or PRK. By exploring the feasibility of inducing controlled alterations in corneal curvature, this

thesis aims to quantitatively investigate the effectiveness and safety of such an approach. The question at hand examines the potential of using EMR to achieve significant shape changes in the cornea, as well as the ability of OCT and subsequent MATLAB processing to accurately quantify the resulting shape change.

Another key question that arises in the context of cornel EMR is whether the treatment poses a risk of collagen structural change. Collagen, being the primary structural component of the cornea, plays a vital role in maintaining its shape and integrity. Understanding the potential impact of EMR on collagen fibrillar orientation is crucial for ensuring the safety and long-term stability of the cornea following the procedure. This thesis aims to investigate and quantify any collagen structural change resulting from EMR using second harmonic generation (SHG) microscopy. By addressing this question, insight can be gained about the potential risks associated with the treatment and develop strategies to minimize collagen disruption, ultimately contributing to the refinement and optimization of corneal EMR.

CHAPTER 2: BACKGROUND

Physiology and Structure of the Eye

To better understand how corneal reshaping can be performed, it is important to understand the physical structure of the eye.

The cornea, a transparent and avascular tissue, is a fundamental component of the human eye. Its structure and organization play a critical role in vision by refracting and focusing light onto the retina. Composed of five distinct layers, namely the epithelium, Bowman's layer, stroma, Descemet's membrane, and endothelium, the cornea exhibits a complex architecture that contributes to its unique properties [6].

The epithelium, the outermost layer of the cornea, acts as a protective barrier against external agents while also maintaining corneal transparency. Consisting of several layers of cells, it undergoes continuous renewal as the outermost cells are shed and replaced by underlying cells. Beneath the epithelium lies Bowman's layer, a thin acellular matrix that provides structural support to the cornea. Although its function is not fully understood, it likely plays a role in maintaining the shape and integrity of the cornea [7].

The stroma is the thickest and middle layer of the cornea, constituting approximately 90% of its thickness. It is composed of a highly organized arrangement of collagen fibers and proteoglycans. The unique structure of the stromal collagen fibers allows for efficient transmission of light through the cornea with minimal scattering, contributing to its transparency. The regular spacing and alignment of collagen fibrils in the stroma contribute to the cornea's mechanical strength and resilience.

Descemet's membrane, located between the stroma and the endothelium, acts as a basement membrane and provides structural integrity to the cornea. It is a thin, acellular layer

composed primarily of collagen and plays a crucial role in preventing corneal swelling and maintaining corneal shape. The endothelium, the innermost layer of the cornea, is a single layer of specialized cells that regulate corneal hydration. It actively pumps fluid out of the stroma, maintaining the optimal balance of water content and corneal transparency.

The structural integrity and organization of the cornea are crucial for its optimal function in vision. Disruptions or abnormalities in corneal structure can lead to various vision problems, such as corneal opacity, astigmatism, or other refractive errors. Understanding the intricate structure of the cornea provides insights into the mechanisms underlying these conditions and guides the development of diagnostic and therapeutic interventions.

The cornea plays a vital role in vision by contributing to the process of focusing light onto the retina. This transparent outermost layer of the eye works in conjunction with other ocular components to ensure optimal visual clarity. Understanding the functioning of the cornea involves examining its refractive properties, the involvement of its different layers, and its interaction with the surrounding structures.

The cornea refracts light by bending light rays as they pass through its curved surface. The curved shape of the cornea allows it to focus light onto the retina, which is responsible for converting light into electrical signals that are then processed by the brain. Through the process of refraction, the cornea contributes to the formation of a clear and sharp image on the retina.

The cornea's interaction with surrounding structures influences its function. The cornea works in conjunction with the lens to focus light on the retina, with the cornea contributing two-thirds of refractive power, while the lens fine-tunes for different distances. Altering corneal curvature and refractive power through surgeries or lenses corrects vision issues. This

understanding guides vision correction and treatment development for corneal conditions and refractive errors, as discussed ahead.

Because the eventual intent of corneal reshaping would be to help correct refractive errors in vision, it is imperative to understand the common issues people have with vision.

Nearsightedness, or myopia, is a common refractive error that causes distant objects to appear blurry to individuals [8]. It is caused because the eyeball is elongated; this difference in shape prevents the incoming light rays from focusing on the retina. The primary cause of nearsightedness is the elongation of the eyeball or excessive curvature of the cornea, which causes light entering the eye to focus in front of the retina instead of directly on it. As a result, the images formed on the retina are blurry, leading to difficulty and seeing distant objects clearly [8].

Nearsightedness can develop gradually during childhood and adolescence, often worsening until the early twenties. It can be influenced by both genetic and environmental factors, such as excessive reading or use of electronic devices, limited time spent outdoors, and a family history of myopia.

Contrary to nearsightedness, farsightedness or hyperopia, is caused because the eyeball is shorter than normal, or the cornea is flatter than usual, which causes light rays to also not focus on the retina. This results in individuals able to see distant objects while having blurred vision for close-up objects. This leads to blurred or distorted vision for objects up close, while objects in the distance may still appear relatively clear. In mild cases of farsightedness, the eyes can compensate by adjusting the lens to bring the image into focus on the retina. However, this can cause eye strain and fatigue, particularly when performing close tasks for extended periods.

Farsightedness may also become more noticeable with age as the eyes' focusing ability diminishes.

Astigmatism is another common refractive error of the eye that causes distorted vision which occurs when the cornea or lens in an individual is misshapen. This irregularity affects the way light is bent or refracted as it enters the eye. The irregular curvature of the cornea or lens causes both vertical and horizontal focal points, leading to distorted or blurred vision. Objects at any distance can appear distorted, and individuals with astigmatism may experience difficulty in perceiving fine details or lines. Astigmatism can occur alone or in combination with other refractive errors, such as the ones aforementioned.

Currently there are several established ways of correcting one's vision. An understanding of the strengths and drawbacks of current approaches to vision correction demonstrates how the novel approach of electromechanically reshaping the cornea can fit into the picture.

Glasses correct vision by focusing light properly on the retina using lenses. Glasses are appealing because they are easy to use, being non-invasive and providing clear vision for a wide range of refractive errors. There are also many different aesthetic options available for consumers; however, aesthetic concerns for wearing glasses can still be a downside for some individuals. Also, eyeglasses can be inconvenient when playing sports or performing other physical activities. Lastly, eyeglasses can be expensive when one factors in maintenance or repair costs.

Contact lenses are another option for vision correction by modifying the way light is focused onto the retina, compensating for the specific refractive error of an individual's eyes. An appealing factor about them is that they can offer a wider range of vision correction because they can help correct higher prescriptions. The fact that contact lenses sit directly on the eye provides

a more natural field of vision than some other vision correction methods such as glasses, which includes the frames in one's peripheral vision. Also, contact lenses are aesthetically appealing because they do not alter one's physical appearance. Wearing contact lenses is also more suitable for people performing physical activities as they do not interfere with such activities. Contact lenses, however, are not without their downsides. Having contact lenses in one's eyes can cause discomfort or dryness because of the fit of the lens or individual sensitivity to contact lens solutions. Also, not following proper contact lens hygiene can lead to bacterial or fungal infections of the eye. Lastly, the cost of contact lenses can be off-putting because of the need for replacement lenses and cleaning solutions.

Other increasingly popular options for vision correction include LASIK (laser-assisted in situ keratomileusis) and PRK (photorefractive keratectomy), which use an excimer laser to reshape the cornea. LASIK and PRK are appealing because they eliminate the need for glasses and contact lenses and are generally performed quickly with minimal discomfort during surgery. Despite the advantages of LASIK and PRK, these interventions pose challenges in safety. Both LASIK and PRK permanently thin the cornea, weakening its biomechanical structure. Furthermore, the LASIK flap introduces complications, as the flap can become infected or melt if the surgery is improperly performed. In addition, LASIK may also cause discomfort and dry eyes following the operation. PRK, on the other hand, can cause persistent corneal epithelial defects that increase susceptibility to infection [9].

Orthokeratology entails wearing rigid lenses while the user is sleeping to gently reshape the cornea. This allows for the user to not have to wear any glasses or traditional contact lenses during the day, which adds to the appeal. Also, orthokeratology could help slow down the rate of myopia progression, which would be beneficial in the long-run. However, like other methods,

orthokeratology has its downsides. Because it resembles a form of contact lenses, the same issues with discomfort and potential infection can occur. Additionally, orthokeratology is suitable for a smaller range of people, so there is a decent chance that a patient may not be a good candidate for the treatment. Lastly, one must adhere to wearing the lenses every night to ensure the process works favorably [10].

Femtosecond laser crosslinking is a non-invasive method that has been recently investigated as an avenue for vision correction. This method uses a low-density plasma to produce a reactive oxygen species, which results in the formation of crosslinks and spatially resolved changes in mechanical properties. Femtosecond laser crosslinking has the potential to broaden the range of patients eligible for permanent vision correction while avoiding the adverse effects associated with current surgical procedures. Furthermore, this method could result in a shorter treatment time, which would benefit the patient. However, because femtosecond laser crosslinking is a relatively new procedure, its availability may be limited at the moment; this along with its expensive cost could be a barrier for patients who are unable to afford such a treatment. Also, because the treatment is new there is a lack of long-term data, so the treatment's long-term potential complications are not yet well understood [11].

Corneal rings are also used for vision correction, particularly in individuals with keratoconus, which causes the cornea to become thin and bulge outward. By implanting the rings in the cornea, the cornea can be flattened, which reduces the cone-shaped bulging caused by keratoconus. Corneal rings are replaceable and can be replaced if necessary; also, the recovery time is short. These factors make it a desirable method of vision correction. Corneal rings come with its limitations: it may not be suitable for people with very thin corneas or if an individual's keratoconus has progressed too far. Also, some patients may not receive the visual acuity they

desired, so an adjustment surgery may be required. Because corneal rings need to be implanted during a surgery, there could be other complications such as infection or eye irritation as well [12].

Current Electrochemical Therapies

Electrochemical reshaping treatments work by applying a controlled electrical potential to tissue, inducing shape changes without the need for invasive surgery. When a potential is applied across a specimen, the potential causes redox reactions within the tissues, leading to localized pH changes that transiently alter the tissue's stress response. This leads the tissue to change shape in response to the deformation and restoring the physiological pH environment locks the new form of the tissue. By carefully controlling the electrical parameters, electrochemical reshaping treatments offer the potential for a noninvasive approach to targeted and controlled tissue reshaping.

On a molecular level, EMR operates through the protonation of immobilized ions within the glycosaminoglycan (GAG) matrix. A study titled "Controlled-Potential Electromechanical Reshaping of Cartilage" proposes that the primary mechanism responsible for the shape change during EMR is the acidification at the anode and the subsequent diffusion of protons into the tissue. This results in the protonation of immobilized anions within the GAG matrix of the tissue that neutralizes the fixed charges and disrupts the ionic-bonding network of the matrix. A change in the ionic-bonding network alters the structural integrity of the tissue, exhibiting stress relaxation in regions of increased internal stress. The re-establishment of the pH to physiological pH restores the fixed-charge density of the ionic-bonding matrix, leading to a sustained shape change of the tissue [13].

Another study titled “Electrochemical treatment of ex vivo human abdominal skin and potential use in scar management: A pilot study” postulates that ECT can be used in combination with intralesional injections of wound healing modulators in the skin. By softening the dense tissue matrix, ECT can potentially enhance the dermis's ability to receive and absorb therapeutic agents. With its potential as an adjunct therapy for tissue remodeling, ECT holds promise for enhancing the effectiveness of treatments aimed at correcting fibrotic collagen and improving tissue function and appearance [14].

Electrochemical therapies induce changes in pH within the targeted tissues; this leads to electrolysis, which is the splitting of water molecules into hydrogen (H^+) and hydroxide (OH^-) ions. This results in alterations in the local pH environment surrounding the electrodes.

The extent of pH changes during electrochemical therapies varies depending on several factors, including the electrical potential applied, duration of the application, the composition of the surrounding fluid, and the buffering capacity of the surrounding tissue or culture medium. The electrode design and materials also affect the pH landscape because different materials exhibit different electrochemical properties.

Several studies have therefore investigated the effects of pH when dealing with EMR of tissue. The study “In-depth analysis of pH-dependent mechanisms of electromechanical reshaping of rabbit nasal septal cartilage” links local tissue pH changes to tissue damage and shape change within the context of EMR. The findings suggest that higher voltage or a longer application time lead to increased diffusion and localized concentrations of redox products, which contribute to the observed phenomena. A limitation to this study however is that the pH values outside of the buffer’s range may have likely not been accurately quantifiable because of

the use of a single pH indicator; hence, the study advocates for the use of multiple pH indicators [15].

Furthermore, the study “Electrochemical treatment of ex vivo human abdominal skin and potential use in scar management: A pilot study” also investigates the effects of pH changes caused by electrochemical treatments in skin. The electrochemical reaction in the study generated pH gradients within the skin tissue by producing hydroxide ions at the cathode and hydrogen ions at the anode, leading to localized biophysical changes. The study suggests that electrochemical treatment modifies the abdominal dermal pH, stimulating wound healing and aiding in collagen fiber reorganization, and the study's pH mapping results indicate that increasing voltage expands the treatment area. This demonstrates that dosimetry parameters can be adjusted to target specific depths and areas of cutaneous tissue [14].

Additionally, the study “Controlled-Potential Electromechanical Reshaping of Cartilage” reveals that electromechanical reshaping is achieved through the generation of localized, low-pH gradients within the tissue. This leads to chemically induced stress relaxation, where fixed negative charges in the proteoglycan matrix become protonated. Rebalancing to physiological pH restores the fixed negative charges, resulting in remodeled cartilage that maintains the shape defined by the reshaping jig. By carefully controlling the electrolysis conditions, predictable and reproducible reshaping of ex vivo tissue with minimal cell mortality can be achieved. These findings position EMR as a potentially transformative, cost-effective surgical therapy that can be implemented at the point of care. Furthermore, when physiological pH is restored after EMR, the remodeled cartilage regains its fixed-charge density and exhibits physical properties similar to untreated tissues, which can have further implications [13].

The findings of these studies highlight the importance of pH control during EMR. Maintaining specific pH ranges is crucial to ensure optimal outcomes and minimize potential tissue damage.

Understanding the cellular responses that occur during EMR is essential for comprehending the underlying mechanisms and optimizing such an approach. One study titled "Survival of Chondrocytes in Rabbit Septal Cartilage after Electromechanical Reshaping" investigates the viability and survival of chondrocytes following electromechanical reshaping procedures. After analyzing the survival of chondrocytes using various techniques, including histological examination and cell viability assays, the findings demonstrate that electroforming can induce cell injury; however, careful selection of voltage and application time can achieve clinically relevant shape changes while selectively preserving cells. By limiting the application of electric voltage to specific regions of stress concentrations, cell injury can be spatially localized. These results suggest that electroforming has therapeutic potential by creating spatially-selective changes in tissue mechanical properties, albeit at the expense of tissue injury in the same site [16].

Another study titled “Quantitative assessment of chondrocyte viability after laser mediated reshaping: a novel application of flow cytometry” focuses on investigating the viability of chondrocytes following laser-mediated reshaping procedures. This gives researchers a better understanding of how reshaping techniques can affect the cells thereafter. The research introduces a novel application of flow cytometry to quantitatively assess chondrocyte viability, providing insights into the cellular response to laser-based reshaping techniques. The application of flow cytometry enables researchers and clinicians to obtain objective and quantitative

measurements of cell viability, facilitating a more precise understanding of the cellular responses to laser-based reshaping [17].

Electromechanical reshaping treatments have demonstrated promising potential not only in corneal reshaping but also in various other tissues, including cartilage, fat, skin, and tendon. These innovative approaches offer non-invasive or minimally invasive alternatives to traditional surgical interventions for tissue modification and reconstruction. The following is a discussion of the emerging EMR treatments for each tissue.

"Controlled-Potential Electromechanical Reshaping of Cartilage" demonstrates the feasibility and effectiveness of controlled-potential electromechanical reshaping in cartilage modification. Through the application of electrical potential, the study shows the ability to induce controlled shape changes in cartilage tissue, promoting tissue remodeling and structural modification. This study highlights the importance of precise control over the electrical potential applied during the reshaping process. By carefully manipulating the electrical parameters, including voltage, duration, and distribution, researchers can achieve desired shape changes while minimizing tissue damage and adverse effects [13].

Another study titled "Electromechanical reshaping of septal cartilage" demonstrates the effectiveness of EMR as a means to reshape septal cartilage in an ex vivo setting. The study investigates the application of EMR to reshape the porcine septal cartilage, offering a non-invasive approach for nasal reconstruction. The research shows the feasibility and effectiveness of EMR in modifying the shape and structure of septal cartilage. By applying a controlled electric potential, the study shows the ability to induce shape changes in the cartilage without the need for invasive surgical procedures. Specifically, the study revealed a strong correlation between shape retention and higher voltage and application time. Like other studies

that have investigated the application of EMR for cartilage, this study underscores the importance of precise control over electrical parameters and highlights the potential applications of EMR in septal cartilage reconstruction and nasal aesthetics [1].

Furthermore, the study “Ex vivo electromechanical reshaping of costal cartilage in the New Zealand white rabbit model” investigates the application of an electric potential to reshape costal cartilage outside of the body, offering insights into the feasibility and potential of this technique. By applying a controlled electric potential, the study assesses the ability to induce shape changes in the costal cartilage tissue. The findings of the study establish EMR as a means of modifying the shape and structure of ex vivo costal cartilage: EMR leads to controlled shape changes in the cartilage samples. By investigating the technique in the New Zealand white rabbit model, the study provides valuable information for further development and optimization of EMR approaches in cartilage reconstruction [18].

In adipose tissue, electrochemical treatments offer possibilities for non-invasive body contouring and fat reduction. Such treatments hold promise as alternatives to invasive and expensive liposuction procedures, allowing for an alternative means for body fat contouring. "Electrochemical Lipolysis Induces Adipocyte Death and Fat Necrosis: In Vivo Pilot Study in Pigs" explores the effects of electrochemical lipolysis on adipocyte death and fat necrosis, with the goal of evaluating its potential as a non-invasive method for fat reduction. Electrochemical lipolysis involves the application of an electric potential to adipose tissue, targeting the adipocytes and inducing their death. The study assesses the extent of adipocyte death and subsequent fat necrosis through histological analysis and other assessments. The findings of the pilot study indicate that electrochemical lipolysis effectively induces adipocyte death and fat necrosis in the treated areas while preserving surrounding tissues. Histological analysis confirms

the occurrence of targeted adipocyte death and fat necrosis, suggesting electrochemical lipolysis is a non-invasive approach for fat reduction. The study provides preliminary evidence of its efficacy in pigs and supports further investigations to explore its clinical applications in human subjects [19].

Electrochemical treatments are also used in dermatology and aesthetic medicine. One study that delves into how electrochemical treatments can be applied to skin is “Electrochemical treatment of ex vivo human abdominal skin and potential use in scar management: A pilot study.” This study investigates the feasibility and potential of electrochemically treating ex vivo human abdominal skin. This pilot study revealed that electrochemically treating the ex vivo abdominal skin led to alterations in the skin cellular response, promoting scar remodeling and reducing scar-related concerns. Due to its dose-dependent and spatially localized effects, it presents an appealing low-cost alternative to existing surgical and pharmaceutical scar revision therapies [14].

EMR enables controlled and localized mechanical and structural changes in tendons. The study “Effects of electromechanical reshaping on mechanical behavior of ex vivo bovine tendon” investigates the feasibility of altering Young's modulus and inducing shape deformation in an ex vivo bovine Achilles tendon model. The results show tissue softening without lengthening during elongation and shortening without compromising compressive stiffness during compression. The findings of the study demonstrate that EMR significantly impacts the mechanical behavior of the ex vivo bovine tendon. EMR leads to changes in tendon stiffness, elasticity, and other structural properties of the tendon [20].

Overall, EMR offers innovative and less invasive strategies for tissue modification in various applications. These approaches hold promise for addressing tissue defects, promoting

functional restoration, and achieving cosmetic improvements. Because treatments have been researched for applications in cartilage, fat, skin, and tendon, the continued advancements in electromechanical technologies and their tailored applications to specific tissue types hold significant potential for future clinical applications.

Electrochemistry

This experiment uses a three electrode setup that allows for precise control and measurement of the electrochemical process [21]. The three electrode configuration is preferable to the two electrode configuration because it allows for more accurate potential control, the separation of electrochemical reactions, and enhanced measurement accuracy. The three electrodes are the working electrode, the reference electrode, and the counter electrode. The working electrode is the primary electrode and is where the electrochemical reaction of interest takes place. The working electrode facilitates the exchange of electrons between the electrochemical system and the solution and is typically made of a conductive material, such as platinum, gold, or glassy carbon. The reference electrode is used to establish a stable and known reference potential in the electrochemical cell. The potential of the working electrode is measured against this reference potential. Commonly used reference electrodes include the silver/silver chloride (AgCl) electrode, the saturated calomel electrode (SCE), and the standard hydrogen electrode (SHE). The counter electrode on the other hand completes the electrical circuit in the cell, providing a pathway for the current to flow. Current in the system flows between the working electrode and the counter electrode; the reference electrode does not participate in the direct flow of current. The counter electrode does not directly participate in the reaction of interest but maintains overall electrical neutrality within the cell by acting as a source

or sink for the electrons involved in the reaction at the working electrode. The counter electrode is typically made of platinum, graphite, or stainless steel.

An important analytical instrument in this experiment is the potentiostat, which controls the working electrode's potential in a three electrode electrochemical cell by applying an appropriate voltage. The potentiostat can generate a specific voltage waveform, such as constant potential, step potential, or cyclic voltammetry, with high accuracy and stability. Potentiostats use a feedback mechanism to maintain the constant potential. This feedback mechanism adjusts the voltage to counteract changes in the electrochemical cell caused by current flow, maintaining the desired potential. In addition, potentiostats are equipped with high-precision amplifiers for accurate current measurement. These amplifiers can measure the current flowing through the working electrode with high sensitivity, allowing detailed analysis of electrochemical processes. In a biomedical context, potentiostats are used to investigate the electron transfer processes in biological systems, enabling the study of electron transfer kinetics, enzyme activity, and electrochemical behavior of biomolecules. This setup enables the study of various electrochemical phenomena and electroanalytical techniques like voltammetry and amperometry.

Using this three electrode configuration, an electrochemical technique called cyclic voltammetry (CV) can be employed. Cyclic voltammetry is an electrochemical technique that is used to determine information about the electrochemical properties (such as oxidation-reduction potential and kinetics) of an analyte in solution by cycling the potential of the working electrode and measuring the resulting current [22]. When carrying out cyclic voltammetry, acid generation or water dissociation processes can occur depending on the composition of the electrolyte solution. Acid generation occurs when the electrolyte solution contains a substance that can undergo an oxidation reaction, leading to the release of protons. During the anodic scan, an

oxidation reaction takes place at the working electrode, resulting in the generation of acid. Water dissociation, meanwhile, occurs when the applied potential is sufficient to drive the oxidation or reduction of water molecules. During the anodic scan, water molecules undergo oxidation at the working electrode, resulting in the generation of oxygen gas and protons, and during the cathodic scan, water molecules undergo reduction, leading to the production of hydrogen gas and hydroxide ions (increasing pH). Phosphate-buffered saline (PBS) is used as the solvent when carrying out cyclic voltammetry experiments. PBS allows for the precise control of the pH in an experimental system because the buffering capacity of phosphate maintains a relatively constant pH even when small amounts of acid or base are added. This is important because the electrochemical behavior of many substances is pH-dependent. Additionally, PBS exhibits a suitable electrochemical window for many redox reactions. The electrochemical window is the range of potentials over which electrochemical reactions can occur without undesirable side reactions or electrode damage.

Finally, to study the charge transfer processes that occur in the electrochemical reactions, this experiment also uses chronocoulometry, which is an electrochemical technique that involves the measurement of current as a function of time when applying a constant potential to the electrochemical cell. This current can be measured by a potentiostat and the current measurement provides information about the amount of charge transferred during the electrochemical reaction. By analyzing the current-time response, the rate of charge transfer can be found.

Optical Coherence Tomography (OCT)

By understanding the fundamental principles and biomedical applications of optical coherence tomography, one can see how such a technique would be desired for studying corneal reshaping.

Optical Coherence Tomography (OCT) is a powerful imaging technique based on low-coherence interferometry. It utilizes the interference of light waves to create high-resolution cross-sectional images of biological tissues. The basic principles of OCT involve splitting light into sample and reference arms. The interference of reflected light waves from the sample arm and the reference arm generates an interferogram, which is analyzed to extract structural information. Technological advancements have significantly improved the resolution, imaging speed, and sensitivity of OCT systems [4], [23].

Different types of OCT systems have been developed, such as Time-Domain OCT (TD-OCT) and Fourier-Domain OCT (FD-OCT). TD-OCT uses a moving reference mirror to obtain depth information, while FD-OCT employs spectrometry to achieve high-speed imaging.

OCT has found widespread biomedical applications in fields such as ophthalmology, cardiology, and gastroenterology. In ophthalmology, OCT enables detailed visualization and diagnosis of retinal diseases, including macular degeneration and diabetic retinopathy.

Broadband Optical Coherence Tomography (OCT) is a variant of OCT that utilizes a broadband light source to achieve high-resolution imaging of biological tissues. Broadband OCT employs a superluminescent diode (SLD) or a femtosecond laser to generate a broad spectrum of wavelengths simultaneously to cover a broadband spectrum [24].

The key characteristic of broadband OCT is its wide spectral bandwidth, which allows for higher axial resolution. The use of a broadband light source results in shorter coherence length, enabling better depth resolution and sharper imaging of tissue structures. This enhanced resolution is particularly advantageous for imaging fine structures and differentiating closely spaced reflectors within tissues.

Furthermore, broadband OCT systems provide higher axial resolution due to the use of a broad spectrum of wavelengths. This enables sharper imaging of tissue structures and better differentiation of closely spaced reflectors within tissues. The increased image resolution allows for more precise identification and characterization of tissue layers, microstructures, and pathological features. Furthermore, the shorter coherence length associated with broadband OCT allows for better depth resolution. This means that fine structures at different depths within the tissue can be visualized with greater clarity and accuracy. It enhances the ability to identify and analyze complex tissue architectures, such as retinal layers in ophthalmology or epithelial layers in dermatology. Additionally, broadband OCT produces images with improved image quality and contrast. The broader spectrum of wavelengths allows for better signal-to-noise ratio, minimizing noise artifacts and improving the overall image quality. This results in clearer visualization of tissue structures and better delineation of boundaries.

Another type of OCT Imaging used is called swept-source OCT. Swept-source Optical Coherence Tomography (SS-OCT) utilizes a swept laser as the light source. Unlike traditional OCT systems that use a broadband light source or a narrowband laser, SS-OCT uses a tunable laser that scans the laser wavelength over a broad spectrum range.

The key characteristic of SS-OCT is its ability to rapidly scan through the wavelength range, typically over tens to hundreds of nanometers, within a short period of time. This rapid wavelength sweeping allows for fast acquisition of A-scans (depth profiles) and enables high-speed imaging.

SS-OCT could be advantageous over traditional OCT systems. Along with the aforementioned imaging speed advantages, the use of a swept laser in SS-OCT provides a long imaging depth range, allowing for imaging of deeper tissues. This is advantageous for

applications that require visualization and assessment of structures beyond the surface layers. This also ties in to the reduced sensitivity roll-off: SS-OCT is less susceptible to sensitivity roll-off compared to some other OCT techniques. Sensitivity roll-off refers to the decrease in signal strength with increasing imaging depth. The longer imaging depth range in SS-OCT helps maintain consistent signal strength throughout the imaging depth [25].

Overall, swept-source OCT has become an important imaging modality due to its fast imaging speed, long imaging depth range, reduced sensitivity roll-off, and its ability to provide valuable insights into various biological tissues and structures.

As briefly mentioned, OCT, being such a powerful tool that is both non-invasive and provides high resolution imaging, has relevant applications in the field of ophthalmology.

OCT is commonly used for imaging the retina, allowing for the visualization of retinal layers and identification of retinal pathologies. It plays a crucial role in the diagnosis, monitoring, and management of retinal diseases, including age-related macular degeneration (AMD), diabetic retinopathy, macular holes, and epiretinal membranes. OCT scans of the retina provide information about the thickness, morphology, and integrity of retinal layers, aiding in disease detection and progression assessment [23].

OCT is utilized to evaluate the optic nerve head and retinal nerve fiber layer (RNFL). It assists in the diagnosis and management of glaucoma, a condition characterized by optic nerve damage. OCT allows for the measurement of RNFL thickness, identifying subtle changes associated with glaucoma progression and guiding treatment decisions.

OCT can image the structures of the anterior segment of the eye, including the cornea, anterior chamber, and lens. It aids in the assessment of corneal shape, corneal thickness, corneal pathologies (such as keratoconus), and anterior chamber angle evaluation for conditions like

angle-closure glaucoma. Additionally, OCT is used for evaluating the crystalline lens and assessing conditions such as cataracts [26].

OCT angiography (OCTA) is a specialized technique that allows for non-invasive visualization of retinal and choroidal vasculature without the need for contrast agents. OCTA provides detailed information about blood flow patterns, enabling the identification of abnormalities such as choroidal neovascularization in AMD or retinal vascular diseases [23].

Second Harmonic Generation (SHG)

An imaging modality that was implemented in this thesis to study the collagen distribution of the cornea before and after EMR was second harmonic generation (SHG). Here we give a brief overview of SHG and its application to this thesis.

Second harmonic generation is a nonlinear optical process in which two photons with the same frequency combine to generate a new photon with twice the frequency, and therefore twice the energy, of the original photons.

The second harmonic frequency is exactly twice the original frequency which corresponds to half the wavelength of the incident light. By detecting the specific frequency of light, SHG microscopy provides high resolution imaging of structures that exhibit SHG properties, such as cornea. This is also due to the fact that structures such as cornea generate a strong second harmonic signal due to its intrinsic nonlinear properties [5].

By visualizing the second harmonic signal, we can observe the organization, orientation, and spatial distribution of the collagen structures within the cornea samples. These observable factors, as well as the high resolution visualization, makes second harmonic generation microscopy viable means to study the structural properties of the cornea.

When imaging the cornea using SHG, several key features and characteristics become apparent.

Firstly, SHG microscopy reveals the highly organized and layered arrangement of collagen fibers within the cornea. Collagen, being the primary component responsible for the cornea's structural integrity, exhibits a distinctive nonlinear optical response when subjected to SHG imaging. The technique allows for the visualization of collagen fibers in a label-free manner, without the need for exogenous contrast agents. The resulting images provide a detailed view of the collagen architecture, revealing the precise arrangement and orientation of the fibers.

Secondly, SHG imaging demonstrates the specific spatial distribution of collagen fibers within different corneal layers. The cornea is composed of various layers, including the epithelium, stroma, and endothelium, each with its unique collagen organization. SHG microscopy enables the distinction and visualization of these layers, highlighting the differences in collagen density, fiber thickness, and spatial arrangement.

Furthermore, SHG imaging can detect and assess alterations or abnormalities in the collagen structure of the cornea. Changes in collagen organization, such as disruptions, irregularities, or increased density, can be indicative of collagen damage, degeneration, or pathologies. By comparing SHG images of healthy corneas with those displaying pathological conditions, researchers can identify and characterize the specific collagen alterations associated with various diseases or external interventions, including corneal reshaping procedures. This allows for a quantitative evaluation of potential collagen damage resulting from such interventions, providing insights into the safety and efficacy of corneal reshaping techniques.

To better understand the application of SHG to corneal analysis, one can examine how previous studies implemented it.

“Second harmonic generation microscopy for quantitative analysis of collagen fibrillar structure” focuses on the application of second harmonic generation microscopy for quantitative analysis of collagen fibrillar structure. The study discusses how SHG can be used to obtain more structural information on the assembly of collagen in corneal tissue than is possible by other microscopy techniques. Specifically, this study quantitatively analyzed the various aspects of collagen fibrillar structure including fibril diameter, orientation, and spatial distribution. Using their developed image analysis algorithms and computational models, the researchers were able to extract the relevant parameters from the SHG images. By analyzing these parameters, researchers were able to gain insights into the organization and properties of collagen in biological contexts [27].

“Noninvasive corneal stromal collagen imaging using two-photon-generated second-harmonic signals” investigated if SHG from femtosecond-pulse lasers could be used to assess corneal stromal collagen organization. From the study the researchers observed that the generated second harmonic signals accurately reflected the organization and distribution of collagen fibers in the cornea.The results demonstrated the potential of SHG for non-invasively assessing corneal health and diagnosing corneal disorders [28].

“Second Harmonic Generation Imaging Analysis of Collagen Arrangement in Human Cornea” focuses on the use of SHG for analyzing the arrangement of collagen in the human cornea. By characterizing and comparing the parameters of fiber alignment, density, and thickness, the researchers were able to gain insights into the variations in collagen organization. The study highlights the significance of SHG imaging as a valuable tool for studying collagen arrangement in the human cornea [29].

"Second harmonic generation imaging of collagen fibrils in cornea and sclera" explores the application of SHG to visualizing and analyzing collagen fibrils and the cornea and sclera of the eye. By analyzing various parameters related to collagen structure, such as fibril diameter, orientation, and packing density, the researchers were able to observe distinct differences and collagen fibril characteristics between the cornea and sclera. The cornea exhibited highly organized and densely packed collagen fibrils, while the sclera showed a looser arrangement with the larger fibril diameters. Therefore by taking advantage of SHG imaging highly detailed visualization, the researchers were able to gain valuable information about the structural differences between these two ocular tissues to contribute to our understanding of ocular biomechanics and diseases related to collagen abnormalities [30].

CHAPTER 3: RESEARCH AND DESIGN METHODS

In this thesis, the effectiveness of corneal EMR was assessed by examining corneal curvature change. In addition, the change in distribution of collagen fibers was also assessed. To this end, OCT and SHG to examine curvature change and collagen structure change respectively. By implementing MATLAB-based strategies and FIJI software analysis, changes in corneal curvature and collagen structure were quantitatively determined. The following section further details the methods used in this thesis:

Experimental Setup

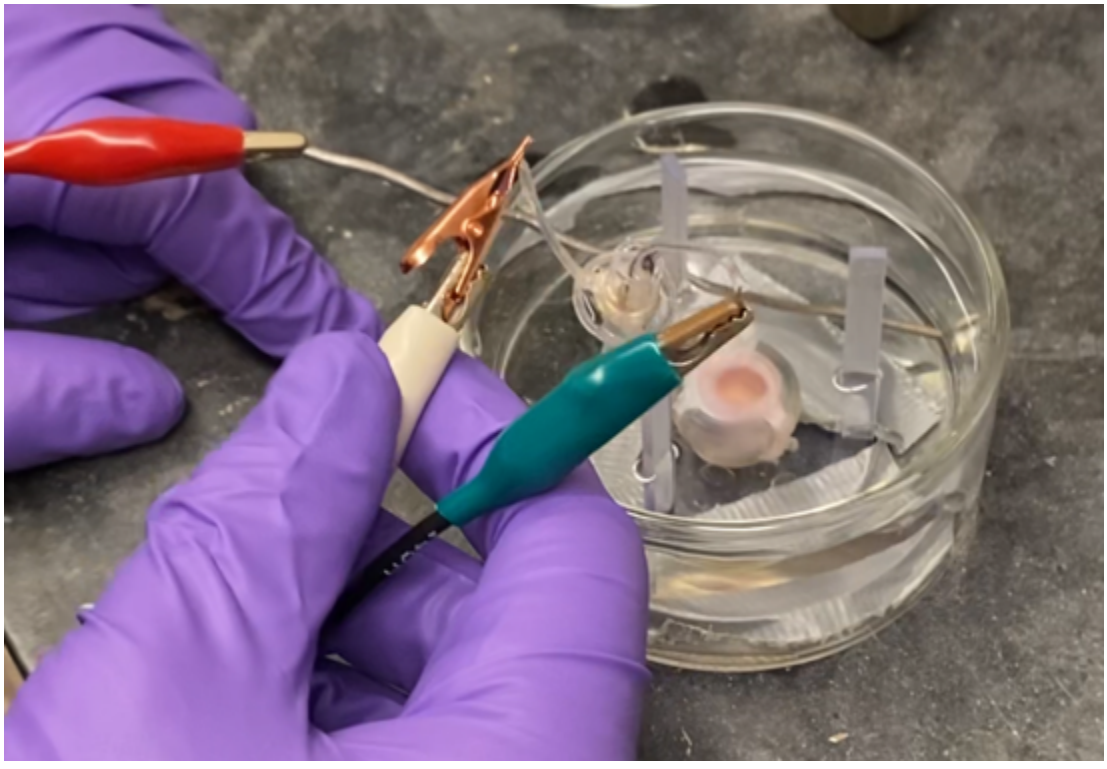

Figure 1. 3-Electrode Setup: This figure shows the 3-electrode setup on a New Zealand white rabbit's eye. The eye is secured in a jig to prevent movement, maintaining the cornea's position for lens contact during treatment. The jig is submerged in phosphate-buffered saline (PBS).

In the electrochemical setup, a three-electrode configuration with a platinum auxiliary wire was utilized. A custom jig immersed in phosphate-buffered saline (PBS) securely housed

the eye specimens, attached to the glassware's base using tape. The electrochemical setup is photographed in **Figure 1**. A concave spherical platinum lens with a 7.486 mm radius of curvature was used for reshaping (**Figure 2** details the fabrication process of the lens). Prior to conducting the electromechanical treatment using the potentiostat, a cyclic voltammogram was generated. During cyclic voltammetry, a pulsing level pH gradient was applied to prevent excessive acidity at the electrode, which could potentially damage the cornea. Subsequently, chronocoulometry was conducted using the potentiostat program, while the working electrode containing the lens was gently placed on the cornea with minimal pressure. The treatment process was considered complete when the anodic current reached 150 mC.

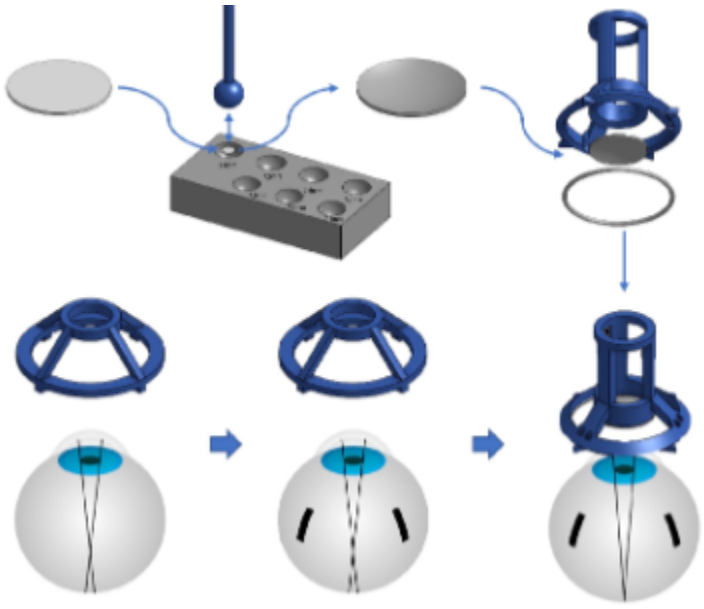

Figure 2. Fabrication of Lens: This figure depicts the manufacturing process of the concave platinum lens. It highlights the lens being shaped in a dapping block before its application as a corneal EMR reshaping lens [31].

New Zealand White rabbit eyes were the preferred choice for corneal reshaping experiments due to their similarity in corneal thickness and curvature to humans, making them a

representative model. This similarity enables a better understanding of treatment outcomes and efficacy. Additionally, New Zealand rabbit eyes are cost-effective and readily-accessible for research purposes.

Methods of Studying Curvature Change

The decision to utilize optical coherence tomography (OCT) as the primary method for studying the shape change in *ex vivo* rabbit eyes holds several compelling justifications. Firstly, OCT offers high-resolution imaging capabilities, allowing for precise and detailed measurements of corneal shape. By capturing cross-sectional images, OCT enables a comprehensive assessment of corneal curvature changes before and after EMR.

Secondly, OCT provides a non-invasive imaging modality, making it suitable for studying *ex vivo* rabbit eyes. The non-contact nature of OCT eliminates the risk of corneal damage or disruption during the imaging process, ensuring the preservation of the corneal tissue's integrity. This non-invasive approach allows for repeated measurements and assessments without altering the natural properties of the rabbit eyes, providing reliable and consistent data for analysis.

Lastly, OCT provides quantitative measurements of corneal shape, facilitating objective analysis and comparison of results. Through image processing software, OCT images can be processed to extract precise curvature parameters such as the radius of curvature. These quantitative measurements enable statistical analysis, inter-sample comparisons, and the establishment of reliable benchmarks for evaluating the efficacy of EMR.

The Spectral Domain Optical Coherence Tomography (SD-OCT) system utilized in this thesis employed an 890 nm Superluminescent Diode (SLD) source with a bandwidth of 150 nm. The system operates at a sample output power of 0.9 mW, ensuring compliance with preset

Maximum Permissible Exposure (MPE) limits. In the detection arm, a diffraction grating with 1200 slits per millimeter (1200 slits/mm) was utilized in conjunction with a Complementary Metal-Oxide-Semiconductor (CMOS) camera, enabling the acquisition of 50,000 A-lines per second. The synchronization of ultrasonic excitation with Optical Coherence Elastography (OCE) acquisition was achieved through a function generator, enhancing the efficiency of detection. A precisely amplified Acoustic Radiation Force Impulse (ARFI) was administered for the specified pulse duration, complemented by the acquisition of 500 A-lines of Doppler OCT to discern tissue responses.

The conventional method for calculating OCT curvature involves identifying the highest peak in a 2D cross-sectional image as the apex and then fitting a circle to determine the radius of curvature. However, practical application is hindered by the strict requirement of precise corneal upright positioning during OCT imaging. Aligning the globe in the jig often introduces minor deviations, resulting in inaccurate curvature values when analyzing the 2D cross sectional OCT images. In response to these challenges, an improved MATLAB-based strategy was adopted. This involved 3D surface reconstruction from 2D cross-sectional OCT images for sphere fitting, thereby mitigating errors and enhancing the precision of radius of curvature calculations. A high-level overview of the MATLAB script can be found in **Figure 3**.

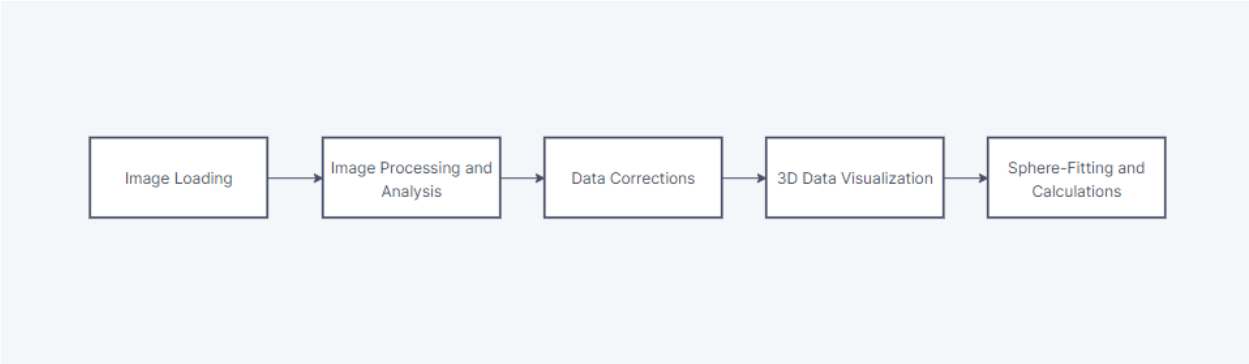

Figure 3. Flow Chart of Curvature Code: This figure provides a concise overview of the MATLAB code's process for calculating corneal curvature from 2D cross-sectional OCT images. It involves five key steps: image loading, processing and analysis, data corrections, 3D visualization, and sphere-fitting calculations.

The 2D cross-sectional OCT images are initially loaded as BMP files and then sequentially renamed for iterative processing. Noise compensation is achieved by consecutively applying a median filter and a Gaussian blur to each image. Subsequently, identification of the corneal surface enables a line to be fitted to each filtered image; from this line the coordinates are able to be extracted and utilized for subsequent 3D reconstruction. **Figure 4** provides a visualization of the filtration and line-fitting process applied to an unfiltered 2D cross-sectional OCT image.

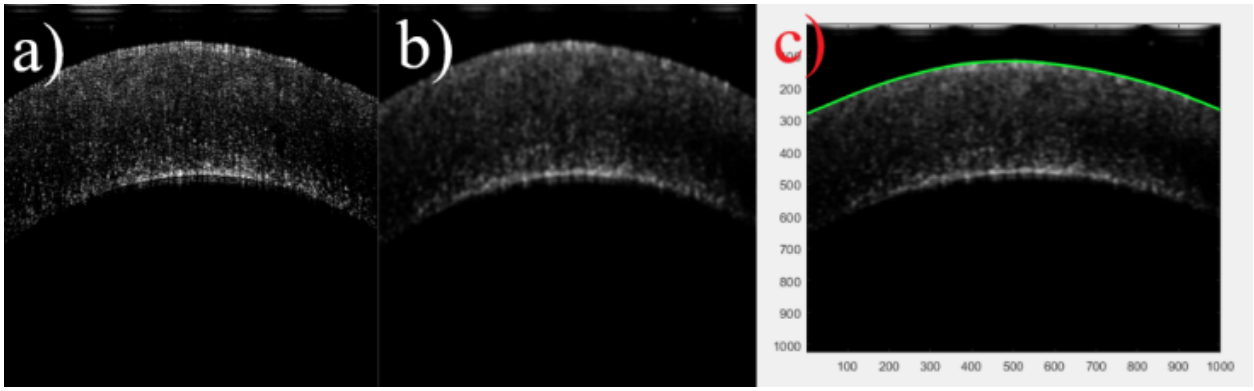

Figure 4. 2D Cross-Sectional Line Fitting: This figure outlines the process of fitting a line to the corneal surface in OCT images for subsequent 3D reconstruction. In a), a raw 2D cross-sectional OCT image is filtered (b) using a median filter of kernel size 2 and a Gaussian blur of 4. A green line is then fitted to the detected surface (c).

MATLAB constructs a 3D data point matrix using coordinates from all the fitted lines in OCT images, with X and Y representing 3D space and Z denoting slice depth. Prior to 3D surface analysis, an intermediary challenge must be addressed: occasional downward shifts are

introduced in OCT images during MATLAB's line-fitting process. To counter these downward shifts, the MATLAB script employs neighboring frame Y-coordinate averaging.The script also employs a 3D median filter for additional surface smoothing, which will help in subsequent sphere-fitting. **Figure 5** demonstrates the impact of averaging and 3D median filtering on the raw data.

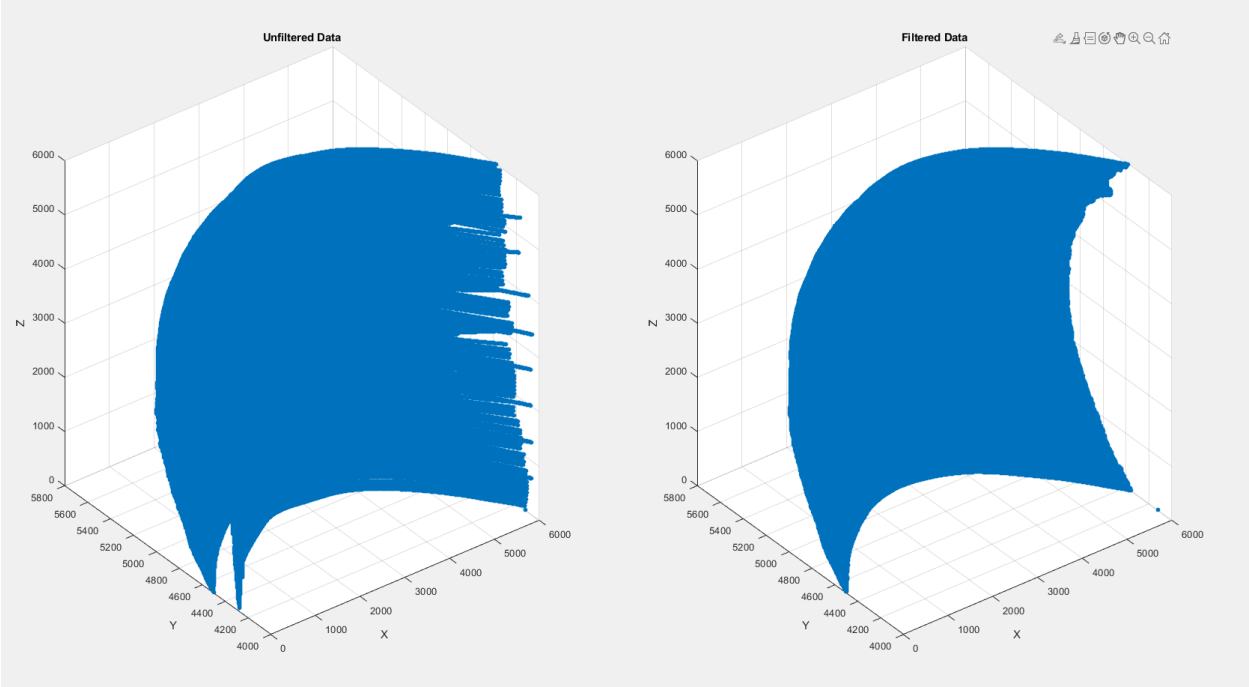

Figure 5. MATLAB 3D Filtering Code: The figure showcases filtering applied to the scatter plot of 3D points for reconstruction. To address misalignment issues, frames in the 2D cross-sectional OCT image folder are compared to neighbors, and excessively low frames are averaged. Subsequently, a 3D median filter is employed on the scatter plot, yielding a smoother surface for eventual sphere fitting.

From the obtained and filtered 3D data points, a sphere-fitting process is executed using an iterative least squares optimization method. This technique aims to find the optimal sphere that best fits the corneal surface curvature. The iterative least squares optimization algorithm initiates with preliminary estimates for the sphere's parameters and progressively refines them to

minimize fitting errors. The preliminary estimate for the center coordinates comes from calculating the mean of the data points, providing initial center coordinates. The initial radius is determined as the maximum distance from the data points to the initial center coordinates. In each iteration, distances between data points and the current sphere's surface are computed, and adjustments to the sphere's parameters are made to minimize the sum of squared distances, leading to convergence and yielding a sphere that accurately fits the data points. Post-sphere fitting, the script visualized the fitted sphere atop scatter plots, highlighting curvature approximation accuracy. The fitted sphere's metrics, including center and radius, were displayed, quantifying corneal curvature. **Figure 6** illustrates an example result from the sphere-fitting.

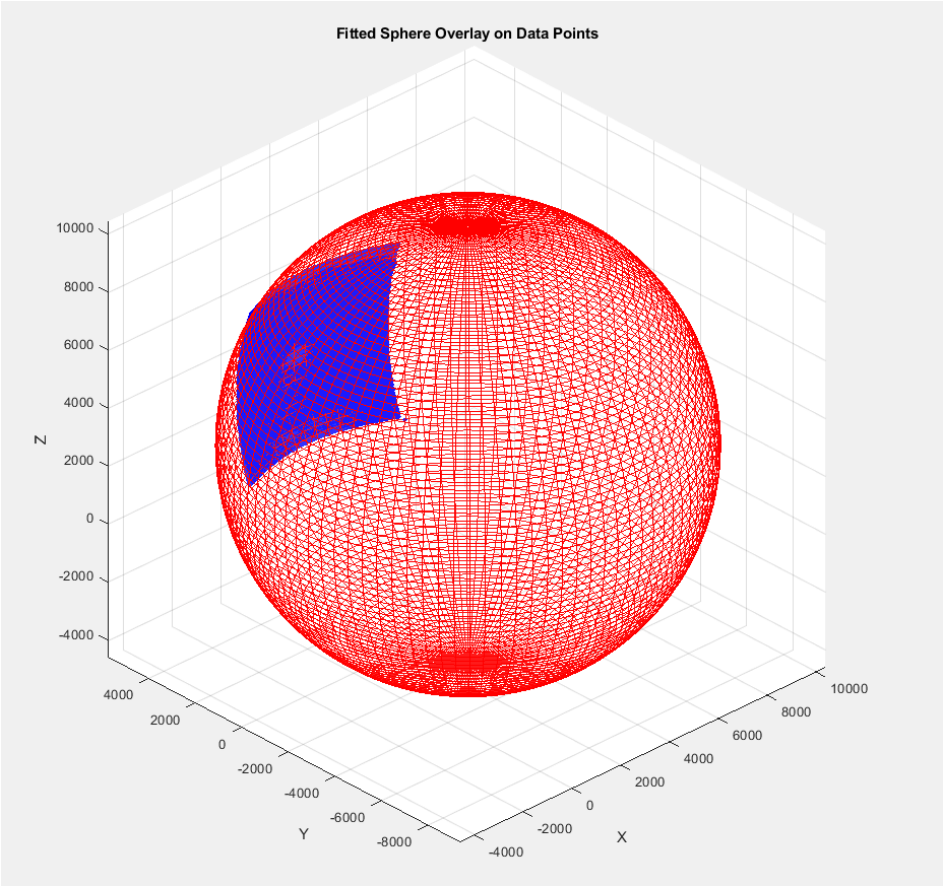

Figure 6. Fitted Sphere Example: This figure demonstrates the fitting of the filtered surface to a sphere using the least squares method. After fitting the sphere, MATLAB displays the sphere's center coordinates and radius of curvature. This example shows the 3D reconstruction of the platinum lens (r = 7.486 mm).

To ensure accurate measurements from this MATLAB script, validation is carried out using a known-size nylon ball (r = 7.935 mm). **Figure 7** depicts OCT imaging of the nylon ball utilized for calibrating the MATLAB script**.**

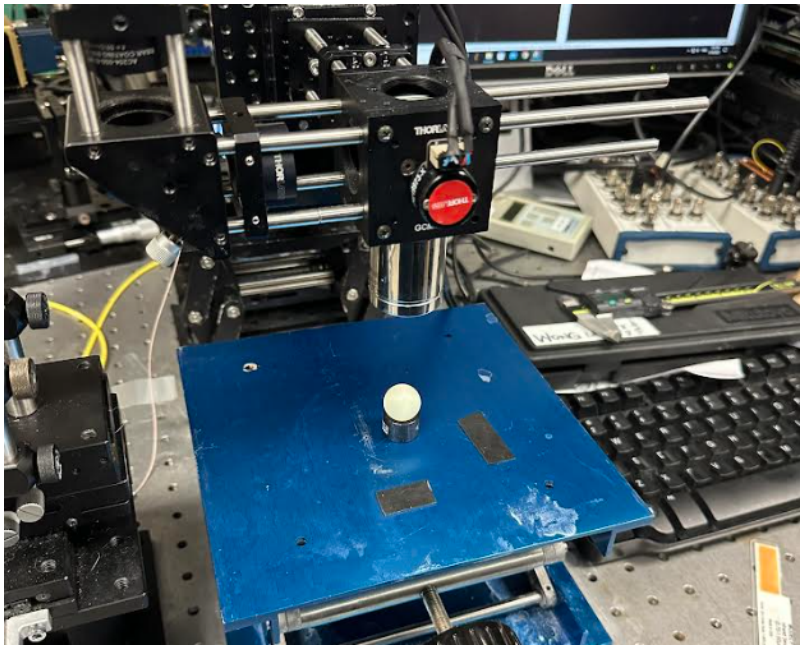

Figure 7. Calibration of System: OCT imaging is performed on a known-radius nylon ball (r = 7.935 mm), validating the MATLAB script's quantification for accurate corneal curvature assessment.

After the curvature values of pre-EMR and post-EMR were gathered from running the MATLAB script on 2D cross-sectional OCT images, a Wilcoxon-signed rank test was performed to determine if there is any statistically significant increase in curvature after corneal EMR. This test is appropriate given the limited sample size (n = 12) for assessing curvature change. The null hypothesis is there is no statistically significant increase in corneal curvature after undergoing

EMR. The alternative hypothesis is that there is a statistically significant increase in corneal curvature after performing EMR.

Methods of Studying Collagen Orientation Change

Employing second harmonic generation (SHG) as the method for assessing collagen structural change in this thesis is supported by several key reasons. Firstly, SHG microscopy offers high-resolution imaging of collagen fibers within the cornea, enabling the visualization of their microstructural organization. Collagen is a critical component of the cornea, and any damage or alterations to its structure can have significant implications for corneal biomechanics and integrity. SHG allows for the direct observation of collagen fibers without the need for exogenous labels or dyes, providing a label-free and non-invasive approach to assess collagen damage.

Secondly, SHG is highly sensitive to changes in collagen architecture and can detect subtle alterations in collagen organization associated with damage or pathology. The nonlinear optical response of collagen to SHG enables the selective imaging of collagen fibers and highlights changes in their arrangement, orientation, and density.

Furthermore, SHG microscopy allows for the examination of collagen damage at a microstructural level. The technique provides detailed spatial information about collagen fiber arrangement and organization, enabling the identification and analysis of specific areas or regions exhibiting damage or abnormalities. This microstructural assessment helps in understanding the extent and distribution of collagen orientation.

Lastly, SHG imaging provides the advantage of being a non-invasive and non-destructive technique, which is particularly important for assessing collagen damage in biological tissues.

This non-invasive nature of SHG microscopy ensures minimal perturbation to the cornea during imaging, allowing for accurate assessment of collagen structural change while maintaining the integrity of the tissue for further analysis.

When using the Leica TCS SP8MP8 Microscope, a 10x objective lens was used. Regarding the settings for second harmonic generation an excitation wavelength of 810 nm and an emission range of 395-415 nm was used. The cornea were imaged at the same depth of 150 μm from the surface of the eye into the tissue. This consistent depth allows for the proper visualization of the collagen structure at an experimentally-determined appropriate depth.

Collagen damage assessment involved comparing SHG images before and after EMR. Quantitative analysis of collagen fiber changes and orientation was pursued. An initial step involved selecting a Region of Interest (ROI) and converting the image to 8-bit format for utilization with the OrientationJ plugin in FIJI software. This plugin employed a cubic spline gradient and local window two-pixel structure tensor to process the image and analyze collagen fiber distribution. The data was filtered by applying a moving average filter in MATLAB and normalized to allow for the comparison between the pre- and post-EMR datasets.

A Kolmogorov-Smirnov (K-S) test was employed to analyze SHG results, comparing pre-EMR and post-EMR collagen fibril distributions extracted from a larger SHG image sample. This test was employed because the resulting collagen fibril distributions followed bimodal distributions. The null hypothesis is that both samples stem from the same larger population distribution, implying collagen fibril orientations are the same. Rejecting the null hypothesis suggests distinct population distributions, implying different fibril orientations between pre-EMR and post-EMR measurements.

CHAPTER 4: RESULTS

Curvature Data

The MATLAB script generated 3D reconstructions from pre-EMR and post-EMR 2D OCT cross-sectional images, followed by sphere-fitting to extract the radius of curvature. **Figure 8** showcases an example of applying the MATLAB script to a corneal surface.

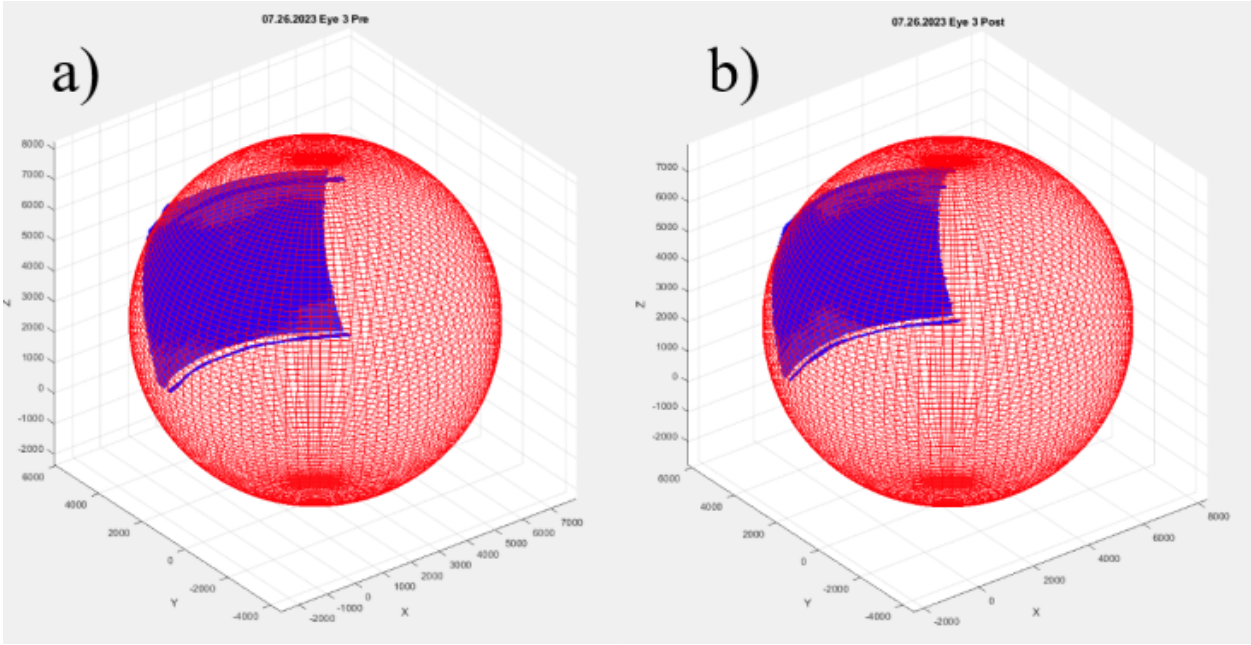

Figure 8. Fitted Sphere for Cornea: This figure displays the fitted sphere for a cornea, where the sphere fitting method largely mitigates the presence of noise. It presents the fitted sphere for a) before (r = 5.2899 mm) and b) after (r = 5.362 mm) electromechanical reshaping.

Following the execution of the MATLAB script on the OCT images of each eye before and after EMR, the radius of curvature was determined. The resulting data is presented in the following table:

Curvature Values Before and After EMR (n=12)

Date	Eye	Pre EMR Radius of Curvature (μm)	Post EMR Radius of Curvature (μm)	Difference
3/14	2	5496.6642	5109.2583	-387.4059
5/3	1	4440.3431	5165.038	724.6949
5/3	2	5382.2002	5557.5604	175.3602
5/3	3	4917.0073	4907.1045	-9.9028
5/3	4	5600.1227	4937.1544	-662.9683
7/26	1	5575.4767	5777.7923	202.3156
7/26	2	5724.8614	7007.4074	1282.546
7/26	3	5289.9	5362.009	72.109
7/26	6	4394.4816	4998.42	603.9384
7/26	7	5169.0134	5858.8106	689.7972
7/26	8	6143.8973	6282.1422	138.2449
8/9	1	4190.8487	4187.2742	-3.5745
Mean		5193.734717	5429.164275	235.4295583
Standard Deviation		597.090669	736.0897795	524.9466716

Three data points were excluded from the table due to procedural errors: two incorrect EMR applications (7/26 Eye 4, 7/26 Eye 5) and one inaccurate post-EMR OCT imaging (3/14 Eye 1).

To better comprehend the tabulated corneal curvature values before and after EMR application, **Figure 9** shows a scatter plot of the curvature data.

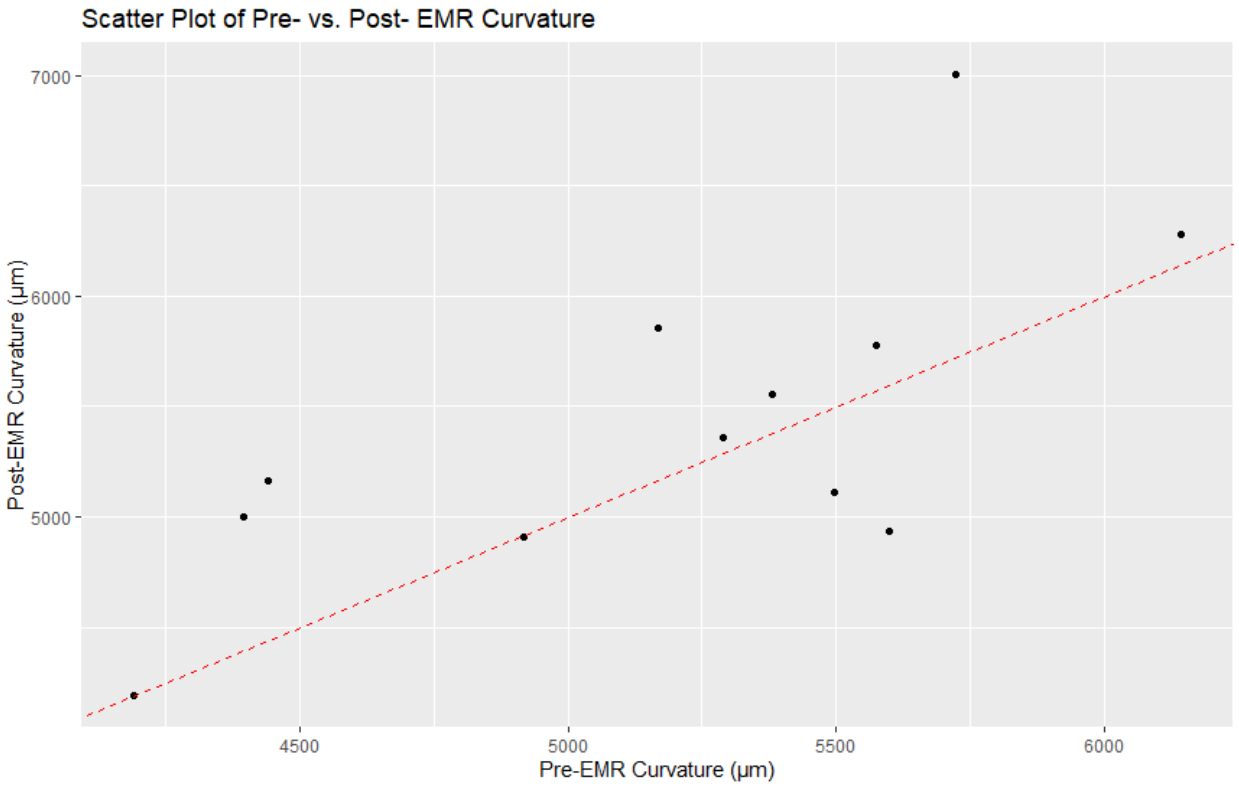

Figure 9. Scatter Plot of Pre- vs. Post- EMR Curvature: a visualization of the corneal curvature changes after EMR application. Points above the line had a desirable, positive increase in curvature.

Collagen Orientation Data

Upon extraction of collagen orientation distributions from pre-EMR and post-EMR regions within SHG images, the data underwent normalization, filtration, and a Kolmogorov-Smirnov test. **Figure 10** showcases an example of the normalization and filtering on an eye before and after EMR application while the following table presents the resulting Kolmogorov-Smirnov p-values alongside their meanings:

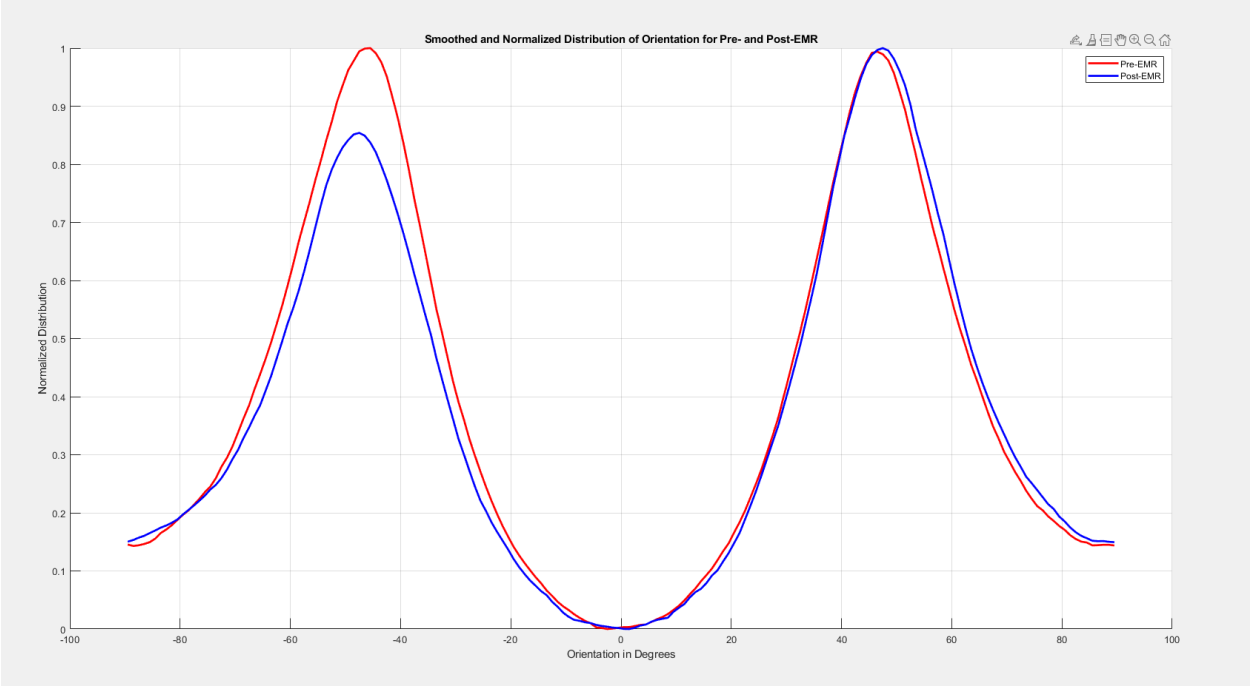

Figure 10. SHG Orientation Graph: This line graph presents the distribution of collagen fiber orientation before and after EMR on 05.03.2023 Eye 3. The pre- and post-EMR datasets are normalized and filtered.

SHG Kolmogorov-Smirnov Results (n = 14)

Date	Eye	Kolmogorov–Smirnov Test p-Value	Result
03/14	1	0.0001	Reject Null Hypothesis (Difference between pre and post SHG)
03/14	2	0.3132	Fail to Reject Null Hypothesis (No Statistically Significant Difference between pre and post SHG)
03/22	1	0.2035	Fail to Reject Null Hypothesis (No Statistically Significant Difference between pre and post SHG)
03/22	2	0.3812	Fail to Reject Null Hypothesis (No Statistically Significant Difference between pre and post SHG)
03/22	3	0.3132	Fail to Reject Null Hypothesis (No Statistically Significant Difference between pre and post SHG)
03/22	4	0.0564	Fail to Reject Null Hypothesis (No Statistically Significant Difference between pre and post SHG)
03/22	5	0.2540	Fail to Reject Null Hypothesis (No Statistically Significant Difference between pre and post SHG)

03/22	6	0.4578	Fail to Reject Null Hypothesis (No Statistically Significant Difference between pre and post SHG)
03/29	1	0.8055	Fail to Reject Null Hypothesis (No Statistically Significant Difference between pre and post SHG)
03/29	2	0.8055	Fail to Reject Null Hypothesis (No Statistically Significant Difference between pre and post SHG)
05/03	1	0.4578	Fail to Reject Null Hypothesis (No Statistically Significant Difference between pre and post SHG)
05/03	2	0.0000	Reject Null Hypothesis (Difference between pre and post SHG)
05/03	3	0.8055	Fail to Reject Null Hypothesis (No Statistically Significant Difference between pre and post SHG)
05/03	4	0.0745	Fail to Reject Null Hypothesis (No Statistically Significant Difference between pre and post SHG)

To qualitatively visualize the effects of SHG on the distribution of collagen orientation, **Figure 11** shows an example on an eye before and after undergoing EMR.

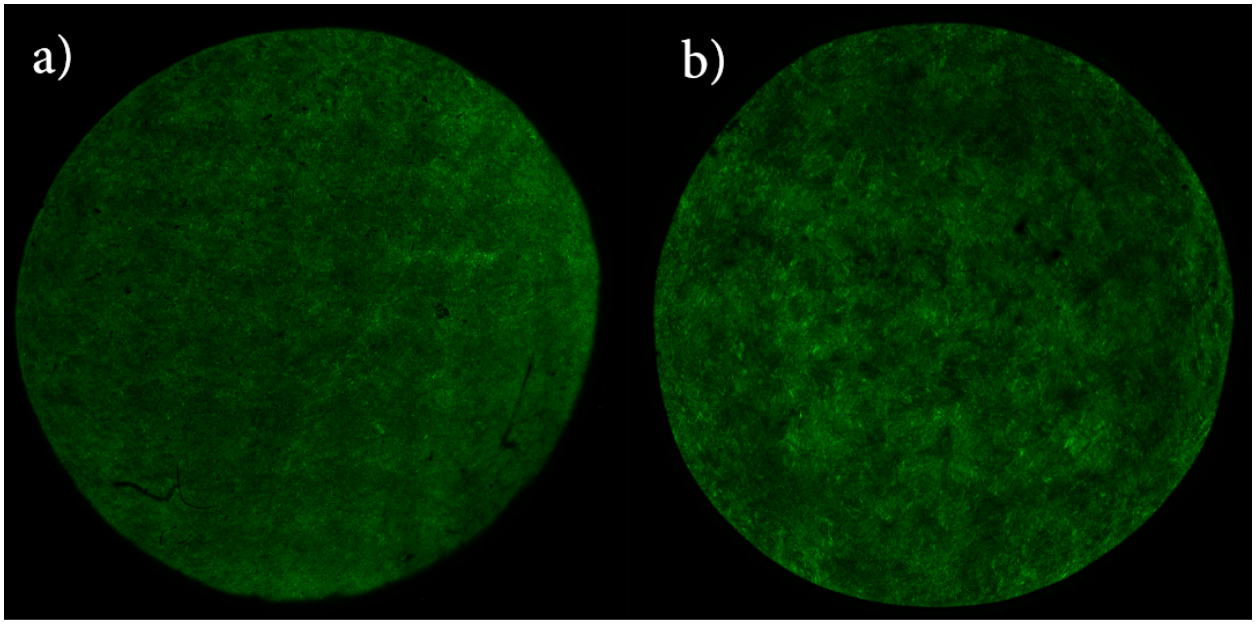

Figure 11. SHG of Cornea: This figure illustrates the qualitative change in collagen orientation on 05.03.2023 Eye 4, comparing a) before and b) after EMR.

CHAPTER 5: DISCUSSION

Summary of OCT Findings

Running a Wilcoxon signed-rank test resulted in a p-value of 0.0647, meaning that conclusive evidence of a significant increase in curvature values cannot be established. This outcome is likely ascribed to experimental errors due to inconsistent corneal lens pressure application, which introduces variability into the experiments. As a result, curvature values at times decreased post-EMR instead of exhibiting exclusively increasing values as expected. To mitigate this limitation, future endeavors could focus on standardizing pressure application. Furthermore, post-treatment curvature values remained below the target of 7.486 mm—the radius of curvature of the platinum reshaping lens—suggesting that an extended EMR application duration could offer a resolution. Implementing both a standardization of pressure and increasing the EMR duration could therefore yield the favorable outcome of aligning corneal curvature more closely with the lens curvature, eventually facilitating controlled diopter changes. Although this study did not establish the efficacy of EMR for corneal applications, this thesis lays the foundation for quantifying curvature results accurately.

OCT Limitations

While utilization of OCT to measure curvature change in corneal reshaping is a valuable approach, it is essential to acknowledge certain limitations that may impact the accuracy and interpretation of the results.

Firstly, the presence of noise in OCT imaging can pose a limitation to accurate data interpretation. Noise artifacts can obscure distinct corneal topography, potentially causing misinterpretation in curvature calculations.Proper noise reduction techniques and advanced

signal processing methods are essential to mitigate these limitations and ensure reliable results in OCT imaging and subsequent MATLAB processing.

Another limitation of OCT in this thesis is that the OCT machine was optimized solely for corneal topography assessment, neglecting stromal changes. To effectively detect stromal variations, the system would require optimization specifically for this purpose.

Lastly, it is imperative that the MATLAB-script is calibrated using the ⅝" nylon ball. Changing scaling settings during OCT imaging without calibration can result in inaccurate curvature measurements after sphere fitting. This greatly affects the reliability of quantitative analyses and the validity of derived curvature measurements. To mitigate this limitation, meticulous attention to calibration procedures is imperative.

Summary of SHG Findings

OrientationJ was used to determine the orientation distribution of the collagen fibers in the SHG images. Plotting the orientation distribution of the collagen fibers against the orientation angle (in degrees) and filtering and normalizing the data (to allow for comparison between pre- and post-EMR SHG images) revealed that the orientation of the collagen fibers is bimodally distributed with average local maxima at −54.32° and 56.77° pre-EMR treatment and −56.06° 51.14° post-EMR treatment. Comparing each eye's collagen fibril orientation distribution pre- and post-EMR treatment using the Kolmogorov-Smirnov test revealed that for all but two eyes (03.14.2023 eye 1 and 05.03.2023 eye 2), the orientation distributions pre- and post-reshaping are not significantly different; however, this could also be due to how the eyes were handled between pre-EMR and post-EMR imaging. This indicates that collagen orientation is minimally affected by EMR treatment, suggesting that the underlying corneal collagen is not damaged during reshaping.

SHG Limitations

Similar to the utilization of OCT in the thesis, there are certain limitations concerning the assessment of collagen orientation change using SHG that should be acknowledged.

For example, the evaluation of collagen damage was primarily based on Second Harmonic Generation (SHG) imaging, which provides information about the structural changes in collagen fibers. However, SHG imaging alone may not be sufficient to fully capture all aspects of collagen damage, such as subtle alterations in collagen organization and potential changes in collagen composition. Complementary techniques, such as histological analysis and biochemical assays, could offer a more comprehensive assessment of collagen damage.

Lastly and briefly, It is crucial to acknowledge that the accuracy of the collagen fiber alignment analysis relied on the quality of the SHG images and the appropriate selection of ROIs. This included selecting ROIs with a high presence of signal.

Overall Limitations

Regarding the thesis as a whole, there may be additional limitations. Firstly, the *ex vivo* nature of the rabbit eye model used in the study might not fully replicate the *in vivo* conditions and physiological responses of the cornea. *Ex vivo* tissue lacks the dynamic interactions with surrounding tissues, ocular fluid dynamics, and ocular surface conditions present in vivo. Hence, the degree of collagen damage observed in *ex vivo* rabbit corneas might differ from that seen in vivo. Future research should therefore consider *in vivo* studies and longer-term follow-ups to assess the stability and long-lasting effects of corneal reshaping using electromechanical methods.

In addition, while this thesis provided valuable insights into the immediate effects of the treatment, long-term reshaping outcomes and potential cumulative effects on collagen integrity

were not explored. Long-term studies are therefore essential to ascertain the permanence of EMR curvature outcomes and to assess the potential for collagen remodeling or repair over time.

CHAPTER 6: CONCLUSION

In summary, this thesis established a robust methodology for quantifying changes in curvature and distribution of collagen orientation resulting from non-invasive electromechanical reshaping of corneas, aimed at rectifying refractive errors. Despite experimental errors such as inconsistent lens pressure and brief EMR duration not yielding the anticipated 7.4 mm corneal curvature, this work sets the groundwork for forthcoming corneal EMR research by enabling data quantification and identifying possible sources of error. For future *ex vivo* corneal EMR endeavors, simultaneous real-time OCT imaging during application could enhance precision and control, and exploring intact globe reshaping could serve as the next step before transitioning to *in vivo* studies. However, assessing the sustained effects of corneal curvature changes post-EMR needs to be investigated to elucidate the longevity of the EMR outcomes. Overall, this thesis serves as a foundational reference for advancing research in employing EMR for vision correction applications.

REFERENCES

[1] K.-H. K. Ho, S. H. Diaz Valdes, D. E. Protsenko, G. Aguilar, and B. J. F. Wong, "Electromechanical reshaping of septal cartilage.," *The Laryngoscope*, vol. 113, no. 11, pp. 1916–1921, Nov. 2003, doi: 10.1097/00005537-200311000-00011.

[2] T. T. Pham *et al.*, "The biophysical effects of localized electrochemical therapy on porcine skin.," *J. Dermatol. Sci.*, vol. 97, no. 3, pp. 179–186, Mar. 2020, doi: 10.1016/j.jdermsci.2020.01.006.

[3] A. M. Stokolosa *et al.*, "Electromechanical Cornea Reshaping for Refractive Vision Therapy.," *ACS Biomater. Sci. Eng.*, vol. 9, no. 2, pp. 595–600, Feb. 2023, doi: 10.1021/acsbiomaterials.2c01177.

[4] R. M. Werkmeister, H. Stegmann, V. A. Dos Santos, D. Schmidl, and L. Schmetterer, "[Cornea Imaging by Optical Coherence Tomography - Historical Aspects and Most Recent Technical Developments].," *Klin. Monatsbl. Augenheilkd.*, vol. 235, no. 12, pp. 1342–1351, Dec. 2018, doi: 10.1055/a-0749-8947.

[5] A. Aghigh, S. Bancelin, M. Rivard, M. Pinsard, H. Ibrahim, and F. Légaré, "Second harmonic generation microscopy: a powerful tool for bio-imaging.," *Biophys. Rev.*, vol. 15, no. 1, pp. 43–70, Feb. 2023, doi: 10.1007/s12551-022-01041-6.

[6] D. H. -, "- Physiology of the Eye.," - *Br Med J 1951 Jun 23147201433*, no. 0007-1447 (Print).

[7] M. S. Sridhar, "Anatomy of cornea and ocular surface.," *Indian J. Ophthalmol.*, vol. 66, no. 2, pp. 190–194, Feb. 2018, doi: 10.4103/ijo.IJO_646_17.

[8] U. Schiefer, C. Kraus, P. Baumbach, J. Ungewiß, and R. Michels, "Refractive errors.," *Dtsch. Arzteblatt Int.*, vol. 113, no. 41, pp. 693–702, Oct. 2016, doi:

10.3238/arztebl.2016.0693.

[9] R. J. Ambrósio and S. Wilson, “LASIK vs LASEK vs PRK: advantages and indications.,” *Semin. Ophthalmol.*, vol. 18, no. 1, pp. 2–10, Mar. 2003, doi: 10.1076/soph.18.1.2.14074.

[10] H. A. Swarbrick, “Orthokeratology review and update.,” *Clin. Exp. Optom.*, vol. 89, no. 3, pp. 124–143, May 2006, doi: 10.1111/j.1444-0938.2006.00044.x.

[11] A. K. Riau *et al.*, “Femtosecond laser-assisted stromal keratophakia for keratoconus: A systemic review and meta-analysis.,” *Int. Ophthalmol.*, vol. 41, no. 5, pp. 1965–1979, May 2021, doi: 10.1007/s10792-021-01745-w.

[12] T. E. Burris, “Intrastromal corneal ring technology: results and indications.,” *Curr. Opin. Ophthalmol.*, vol. 9, no. 4, pp. 9–14, Aug. 1998, doi: 10.1097/00055735-199808000-00003.

[13] B. M. Hunter *et al.*, “Controlled-Potential Electromechanical Reshaping of Cartilage.,” *Angew. Chem. Int. Ed Engl.*, vol. 55, no. 18, pp. 5497–5500, Apr. 2016, doi: 10.1002/anie.201600856.

[14] D. M. Hutchison *et al.*, “Electrochemical treatment of ex vivo human abdominal skin and potential use in scar management: A pilot study.,” *Scars Burns Heal.*, vol. 7, p. 2059513120988532, Dec. 2021, doi: 10.1177/2059513120988532.

[15] E. C. Kuan, A. A. Hamamoto, C. T. Manuel, D. E. Protsenko, and B. J. F. Wong, “In-depth analysis of pH-dependent mechanisms of electromechanical reshaping of rabbit nasal septal cartilage.,” *The Laryngoscope*, vol. 124, no. 10, pp. E405-410, Oct. 2014, doi: 10.1002/lary.24696.

[16] D. E. Protsenko, K. Ho, and B. J. F. Wong, “Survival of chondrocytes in rabbit septal cartilage after electromechanical reshaping.,” *Ann. Biomed. Eng.*, vol. 39, no. 1, pp. 66–74, Jan. 2011, doi: 10.1007/s10439-010-0139-7.

[17] A. Rasouli, C.-H. Sun, R. Basu, and B. J. F. Wong, “Quantitative assessment of chondrocyte viability after laser mediated reshaping: a novel application of flow cytometry.,” *Lasers Surg. Med.*, vol. 32, no. 1, pp. 3–9, 2003, doi: 10.1002/lsm.10142.

[18] K. Badran, C. Manuel, C. Waki, D. Protsenko, and B. J. F. Wong, “Ex vivo electromechanical reshaping of costal cartilage in the New Zealand white rabbit model.,” *The Laryngoscope*, vol. 123, no. 5, pp. 1143–1148, May 2013, doi: 10.1002/lary.23730.

[19] T. T. Pham *et al.*, “‘Electrochemical Lipolysis Induces Adipocyte Death and Fat Necrosis: In Vivo Pilot Study in Pigs’.,” *Plast. Reconstr. Surg.*, May 2023, doi: 10.1097/PRS.0000000000010645.

[20] T. D. Nguyen, A. C. Hu, D. E. Protsenko, and B. J. F. Wong, “Effects of electromechanical reshaping on mechanical behavior of exvivo bovine tendon.,” *Clin. Biomech. Bristol Avon*, vol. 73, pp. 92–100, Mar. 2020, doi: 10.1016/j.clinbiomech.2020.01.009.

[21] C. Mann and E. Grunwald, *Electroanalytical Chemistry*, vol. 81. ACS Publications, 1959.

[22] P. M. Monk, *Fundamentals of electroanalytical chemistry*. John Wiley & Sons, 2008.

[23] D. P. Popescu *et al.*, “Optical coherence tomography: fundamental principles, instrumental designs and biomedical applications.,” *Biophys. Rev.*, vol. 3, no. 3, p. 155, Sep. 2011, doi: 10.1007/s12551-011-0054-7.

[24] T. H. Ko *et al.*, “Ultrahigh resolution optical coherence tomography imaging with a broadband superluminescent diode light source,” *Opt. Publ. Group*, vol. 12, pp. 2112–2119, 2004.

[25] A. Yasin Alibhai, C. Or, and A. J. Witkin, “Swept source optical coherence tomography: a review,” *Springer*, vol. 6, pp. 7–16, 2018.

[26] Y. Siddiqui and J. Yin, “Anterior Segment Applications of Optical Coherence Tomography

Angiography.," *Semin. Ophthalmol.*, vol. 34, no. 4, pp. 264–269, 2019, doi: 10.1080/08820538.2019.1620805.

[27] X. Chen, O. Nadiarynkh, S. Plotnikov, and P. J. Campagnola, "Second harmonic generation microscopy for quantitative analysis of collagen fibrillar structure.," *Nat. Protoc.*, vol. 7, no. 4, pp. 654–669, Mar. 2012, doi: 10.1038/nprot.2012.009.

[28] N. Morishige, W. M. Petroll, T. Nishida, M. C. Kenney, and J. V. Jester, "Noninvasive corneal stromal collagen imaging using two-photon-generated second-harmonic signals.," *J. Cataract Refract. Surg.*, vol. 32, no. 11, pp. 1784–1791, Nov. 2006, doi: 10.1016/j.jcrs.2006.08.027.

[29] United States. *Second Harmonic Generation Imaging Analysis of Collagen Arrangement in Human Cornea.*, (Aug. 2015). doi: 10.1167/iovs.15-17129.

[30] M. Han, G. Giese, and J. Bille, "Second harmonic generation imaging of collagen fibrils in cornea and sclera.," *Opt. Express*, vol. 13, no. 15, pp. 5791–5797, Jul. 2005, doi: 10.1364/opex.13.005791.

[31] M. G. Hill, "R01 Research Strategy 2023." 2023.

APPENDIX A: MATLAB SCRIPT

The following is the commented MATLAB code used to 3D reconstruct and analyze the curvature data:

```
% This function serves to filter a folder full of OCT images with a
% specified gaussian sigma and median kernel size. The files are
renamed to
% follow a naming pattern of 0000.bmp, 0001.bmp, 0002.bmp, etc.
function applyFiltersToOCTImages(input_folder, output_folder,
gaussian_sigma, median_kernel_size)
% Create the output folder if it doesn't exist
if ~exist(output_folder, 'dir')
mkdir(output_folder);
end
% Get a list of all files in the input folder
filelist = dir(fullfile(input_folder, '*.bmp'));
% Loop through each image file in the input folder
for n = 1:length(filelist)
% Load the current image
filename = filelist(n).name;
fullfilepath = fullfile(input_folder, filename);
oct_image = imread(fullfilepath);
% Apply median filter
median_filtered_image = medfilt2(oct_image, [median_kernel_size,
median_kernel_size]);
% Apply Gaussian blur
```

```
gaussian_blurred_image = imgaussfilt(median_filtered_image,
gaussian_sigma);
% Save the filtered image with a new filename
[~, name, ext] = fileparts(filename);
new_filename = sprintf('%04d%s', n-1, ext);
new_fullfilepath = fullfile(output_folder, new_filename);
imwrite(gaussian_blurred_image, new_fullfilepath);
end
end

% Initializes the variables used in the curvature calculations
foldername = '';
yres = 6.65795e3/1024; % sets the y-resolution in microns
xres = 6; % sets the x-resolution in microns
% Finds out how many OCT images are in the folder
bmpFiles = dir(fullfile(foldername, '*.bmp'));
totalpic = numel(bmpFiles);
nstart =1;
path = [foldername sprintf('%.4d.bmp',0)];
data = imread(path);
[depth,xlines] = size(data);
grim_array = zeros(totalpic,xlines);
if(isempty(grim_array))
grim_array = zeros(totalpic,xlines);
else
[tpic,txline] = size(grim_array);
```

```
if(tpic~=totalpic||txline~=xlines)
grim_array = zeros(totalpic,xlines);
end
end
upoffset = 1;
btmoffset = depth;
bseg2 = 0;
data_time = zeros(depth,xlines,totalpic);
% Preallocation optimization
all_x0 = ones(1,totalpic);
all_y0 = ones(1,totalpic);
all_z0 = ones(1,totalpic);
% Loop through each image, segment, and extract the coordinates. An
image
% of each fitted line is displayed for visual feedback to ensure the
lines
% are fitting the corneal surface properly.
for n=nstart:totalpic
display(n);
path = [foldername sprintf('%.4d.bmp',n-1)];
data = single(imread(path));
data_time(:,:,n) = data;
grimup_in = upoffset*ones(1,xlines);
grimdown_in = btmoffset*ones(1,xlines);
direction = 1;
distance = 2;
```

```
if(bseg2)
direction = 1;
end
[ grim_tmp ] = SinSideSegmentation(
medfilt2(data,[2,2]),grimup_in,grimdown_in,direction,distance);
if(bseg2)
grimup_in = upoffset*ones(1,xlines);
grimdown_in = grim_tmp;
direction = 1;
distance = 2;
[ grim_top ] = SinSideSegmentation(
medfilt2(data,[2,2]),grimup_in,grimdown_in,direction,distance);
grim_cornea = smooth((grim_top+grim_tmp)/2,0.2,'lowess');
else
grim_cornea = smooth(grim_tmp,0.2,'lowess');
end
grim_correct = depth - grim_cornea';
grim_array(n,:) = grim_cornea';
figure(1);
imagesc(data);
colormap(gray);
hold on;
plot(grim_cornea,'-r','LineWidth',2);
hold on;
plot(grim_array(n,:)','-g','LineWidth',2);
hold off;
```

```
y0 = grim_correct*yres;
x0 = (0:xlines-1)*xres;
% Store the data for the combined 3D plot
all_x0 = [all_x0, x0];
all_y0 = [all_y0, y0];
all_z0 = [all_z0, repmat(n * 6, size(x0))];
end

% The following section of code corrects the downward shifts in the
data
% Assuming you have your all_x0, all_y0, and all_z0 data
% Calculate the number of frames
numFrames = numel(all_x0) / 1000;
% Reshape the data into frames
x0_frames = reshape(all_x0, 1000, numFrames);
y0_frames = reshape(all_y0, 1000, numFrames);
z0_frames = reshape(all_z0, 1000, numFrames);
% Calculate the mean or median of each frame
mean_x0_frames = mean(x0_frames, 1);
mean_y0_frames = mean(y0_frames, 1);
mean_z0_frames = mean(z0_frames, 1);
% Identify frames with downward shifts (dips)
threshold = 3950; % Adjust as needed based on the y0 range
dipped_frames = find(mean_y0_frames < threshold);
% Move frames to the average position of previous and next frames
for i = dipped_frames
```

```
if i > 1 && i < numFrames
y0_frames(:, i) = (y0_frames(:, i - 1) + y0_frames(:, i + 1)) / 2;
elseif i == 1
y0_frames(:, i) = y0_frames(:, i + 1);
else
y0_frames(:, i) = y0_frames(:, i - 1);
end
end
% Reshape the corrected frames back into a single array
corrected_all_y0 = reshape(y0_frames, 1, []);
% Perform 3D median filtering on the data
filter_size = [5, 5, 5]; % Adjust the filter size as needed
filtered_all_x0 = medfilt3(x0_frames, filter_size);
filtered_corrected_all_y0 = medfilt3(y0_frames, filter_size);
filtered_all_z0 = medfilt3(z0_frames, filter_size);
% Reshape the filtered frames back into single arrays
filtered_all_x0 = reshape(filtered_all_x0, 1, []);
filtered_corrected_all_y0 = reshape(filtered_corrected_all_y0, 1, []);
filtered_all_z0 = reshape(filtered_all_z0, 1, []);
% Create a 3D scatter plot of the filtered data
figure;
scatter3(filtered_all_x0, filtered_corrected_all_y0, filtered_all_z0,
'.');
xlabel('X');
ylabel('Y');
zlabel('Z');
```

```
title('3D Scatter Plot of Filtered Data');
% Optional: Rotate the plot to view it from different angles
view(3);

% The following performs a least squares sphere fit algorithm with
initial
% guess computations and generates sphere-fitting graphs
% Combine x, y, and z coordinates to form the 3D data points
data_points = [filtered_all_x0', filtered_corrected_all_y0',
filtered_all_z0'];
% Calculate the mean of the data points as an initial guess for the
center
initial_center_guess = mean(data_points);
% Calculate the initial radius as the maximum distance from the center
distances = sqrt(sum((data_points - initial_center_guess).^2, 2));
initial_radius_guess = max(distances);
% Initial guess for center and radius
initial_guess = [initial_center_guess, initial_radius_guess];
% Use lsqnonlin to fit the sphere to the data
options = optimoptions('lsqnonlin', 'Display', 'iter');
sphere_params = lsqnonlin(@(params) sphere_residuals(params,
data_points), initial_guess, [], [], options);
% Extract the center and radius of curvature from the fitted sphere
center_x = sphere_params(1);
center_y = sphere_params(2);
center_z = sphere_params(3);
```

```
radius_of_curvature = sphere_params(4);
disp(['Center: (', num2str(center_x), ', ', num2str(center_y), ', ',
num2str(center_z), ')']);
disp(['Radius of Curvature: ', num2str(radius_of_curvature)]);
% Create a 3D scatter plot of the data points
scatter3(filtered_all_x0, filtered_corrected_all_y0, filtered_all_z0,
10, 'b', 'filled');
hold on;
% Plot the fitted sphere
[x_sphere, y_sphere, z_sphere] = sphere(100);
x_sphere = x_sphere * radius_of_curvature + center_x;
y_sphere = y_sphere * radius_of_curvature + center_y;
z_sphere = z_sphere * radius_of_curvature + center_z;
mesh(x_sphere, y_sphere, z_sphere, 'EdgeColor', 'r', 'FaceAlpha',
0.1);
xlabel('X');
ylabel('Y');
zlabel('Z');
title('Fitted Sphere Overlay on Data Points');
legend('Data Points', 'Fitted Sphere');
grid on;
axis equal;
hold off;
% Function for residuals for lsqnonlin
function res = sphere_residuals(params, data)
center_x = params(1);
```

```
center_y = params(2);
center_z = params(3);
radius = params(4);
% Calculate the Euclidean distance between each data point and the
sphere's surface
distance = sqrt((data(:, 1) - center_x).^2 + (data(:, 2) -
center_y).^2 + (data(:, 3) - center_z).^2);
% Subtract the sphere's radius from the calculated distances
% This creates a vector of residuals representing the differences
res = distance - radius;
end
```

APPENDIX B: SWEPT-SOURCE OCT BUILD

In addition to the mentioned experiments, another effort entailed creating a swept-source optical coherence tomography (SS-OCT) device. This involved integrating the key components of a swept-source laser, optical path setup, sample and reference arms, photodetector, signal processing, system control, and software. Precise alignment and calibration were vital for optimal functionality and image quality. The finished system achieved a lateral resolution of 15μm (x-direction), 23μm (y-direction), and an axial resolution of 4.88μm. Here is a detailed description of the main steps involved in building a SS-OCT system:

First, a swept-source laser was acquired. The heart of an SS-OCT system is the swept-source laser, which provides the broadband light source necessary for OCT imaging. In this application, the 1310nm laser has high stability, wide tuning range (100 nm bandwidth), 100kHz sweep rate, 10 μm resolution, and high output power to ensure optimal imaging performance.

Next, the construction of the interferometer was undertaken. However, prior to this step, it was important to ensure that all components were in proper working order. To verify functionality, each optical component was connected to a laser, and the output was observed using an infrared card to confirm the transmission of light. Additionally, the delay line and galvanometers were connected to power supply units and function generators to assess responsiveness and controllability. To achieve high-quality imaging with accurate depth information, precise matching of optical path lengths in the sample and reference arms was crucial. Thus, meticulous measurements were conducted for all fibers, couplers, circulators, and other optical devices to ensure alignment; the measurements are better visualized in **Figure B.1**.

Moreover, during the assembly of different components, special attention was given to disinfecting the fiber optic connection areas.

In the optical path, the light emitted from the swept-source laser was divided by a 99:1 coupler (WD6513A), allocating 99% of the light to the sample arm and 1% to the reference arm. The sample arm allows for the illumination of the target sample, while the reference arm provides a stable reference signal. The direction of light was led by the circulators (1310-50-APC) The two arms are subsequently recombined using a 50:50 coupler (TW1300R5A2), leading to a photodetector. The photodetector captured the interference between the sample and reference beams, enabling the acquisition of OCT signals and subsequent image generation. The configuration of the sample arm, reference arm, and photodetector is essential for achieving accurate and high-quality OCT imaging. The finished interferometer is shown in **Figure B.2**.

Sample Arm: The sample arm delivers light to the target sample and collects the backscattered light for interferometric measurements. It includes the lens for focusing the light (Thorlabs LSM04, <40 μm resolution), scanning mechanisms (such as galvanometer mirrors) for lateral scanning (ThorLabs GVS102), and a collimator to align the light rays into a parallel path, which can be seen in the OCT stand in **Figure B.3**.

Reference Arm: The reference arm provides a stable reference signal for interferometric measurements. It includes a reference mirror (P5-SMF28ER-P01-1) that reflects a portion of the light back into the system. There is also a delay line component (ODL300 OZ Optics) included to account for any minute measurement errors that may occur when matching path lengths, as seen in **Figure B.4**. The path length of the reference arm should be carefully controlled to achieve high axial resolution in the OCT image.

Photodetector: A photodetector (Thorlabs PDB130C) plays a crucial role in a SS-OCT system. It converts the backscattered light from the sample into electrical signals for further processing and analysis. The photodetector's primary purpose is to measure the intensity of the interference signal generated between the reference and sample arms. By detecting the interference fringes, it enables the acquisition of depth-resolved information from the sample. The photodetector's sensitivity, noise performance, and response time are key factors in determining the system's signal-to-noise ratio, dynamic range, and imaging speed.

An issue encountered during the construction of the swept-source OCT system was the lack of an adapter to connect the OCT stand to the cage housing the galvanometer-controlled mirrors. To address this, a custom connection part was designed in SolidWorks, considering the screw configurations and incorporating suitable counter bores. The final connection part was machined from aluminum, ensuring a proper fit and functionality within the system. The engineering drawing of the part can be viewed in **Figure B.5** and its integration to the OCT stand can be seen in **Figure B.3**.

Finally, a computer was utilized for signal processing, data acquisition, and laser clock control. The electrical signals from the photodetector were processed and digitized for analysis. Signal processing algorithms, including Fourier transformation, were employed to extract depth information and generate OCT images. Data acquisition systems were employed to capture and store OCT data for further analysis and visualization. The implemented software for the swept-source OCT system facilitated real-time imaging display.

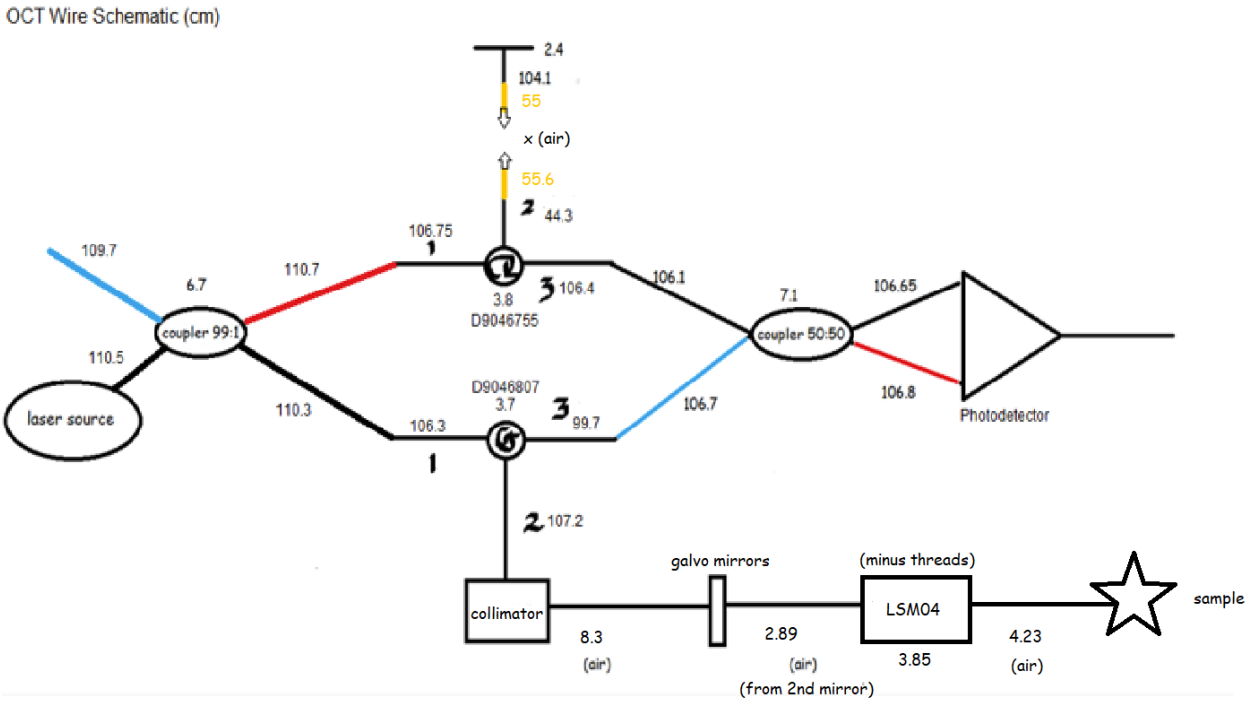

Figure B.1. SS-OCT Schematic: The schematic displays the finalized interferometer. When measuring optical path lengths, it's crucial to account for index of refraction changes because both air and glass are present in the system.

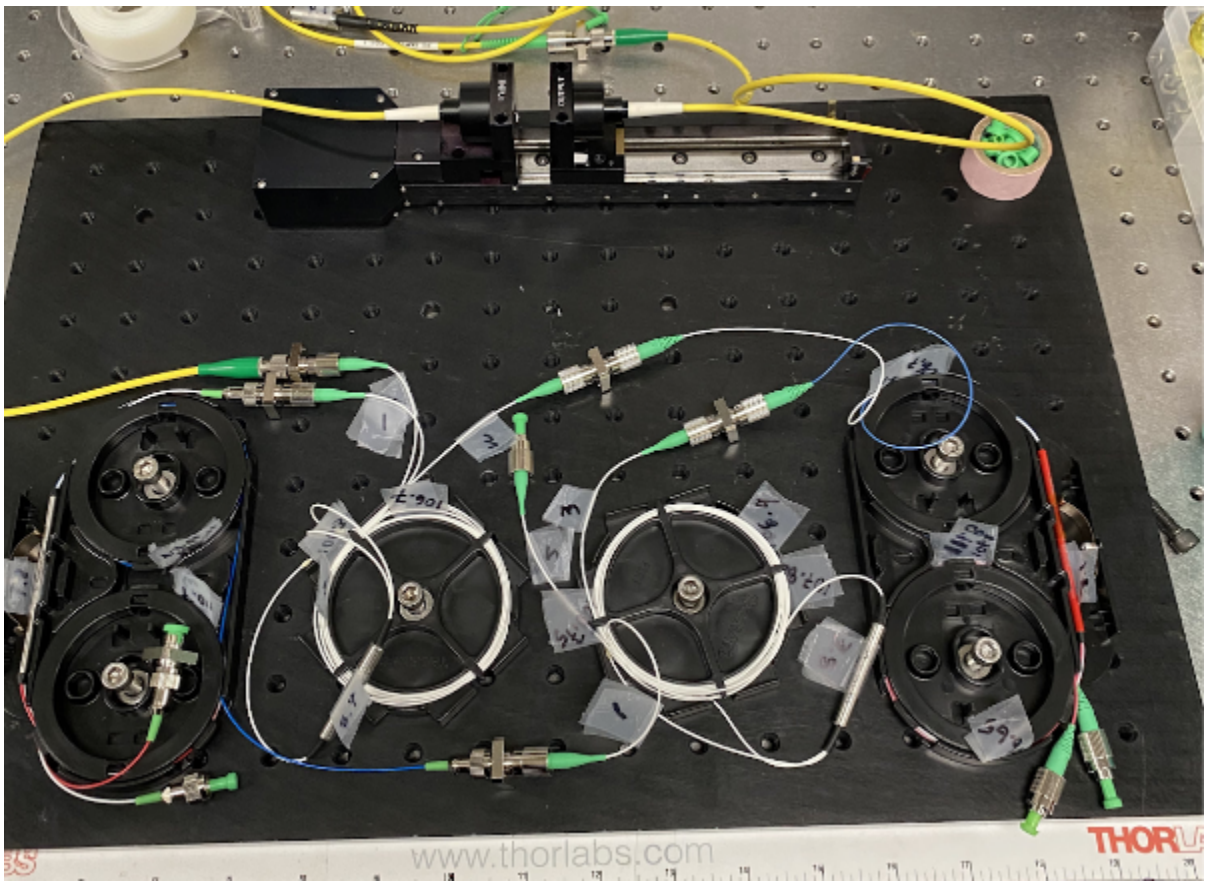

Figure B.2. Interferometer: This figure shows the interferometer positioned on an optical breadboard. The Interferometer follows the SS-OCT Schematic shown in **Figure A.1.**

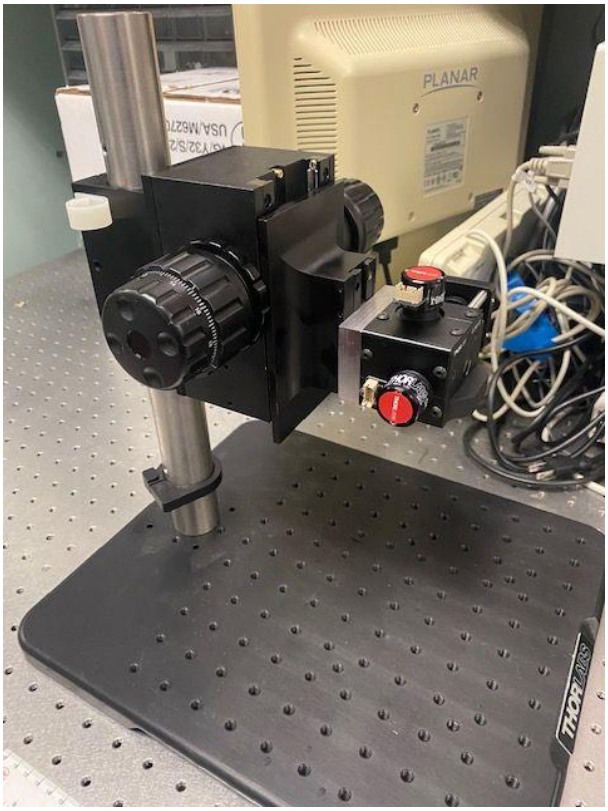

Figure B.3. Assembled SS-OCT Stand: The figure illustrates the employed SS-OCT stand, highlighting the use of a machined aluminum OCT connector component for the setup. This connector aids in ensuring stable and accurate connections within the system.

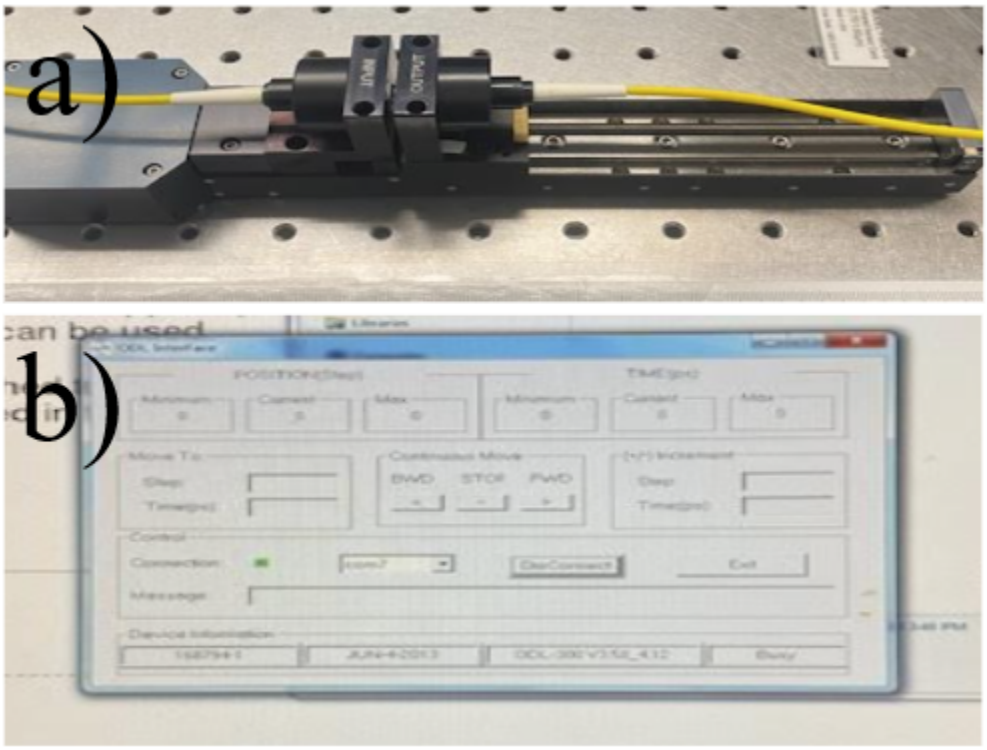

Figure B.4. Delay Line Component: The provided image showcases the a) delay line and b) its corresponding software. The software allows for precise adjustment of the delay line's position, enabling accurate matching of optical path lengths.

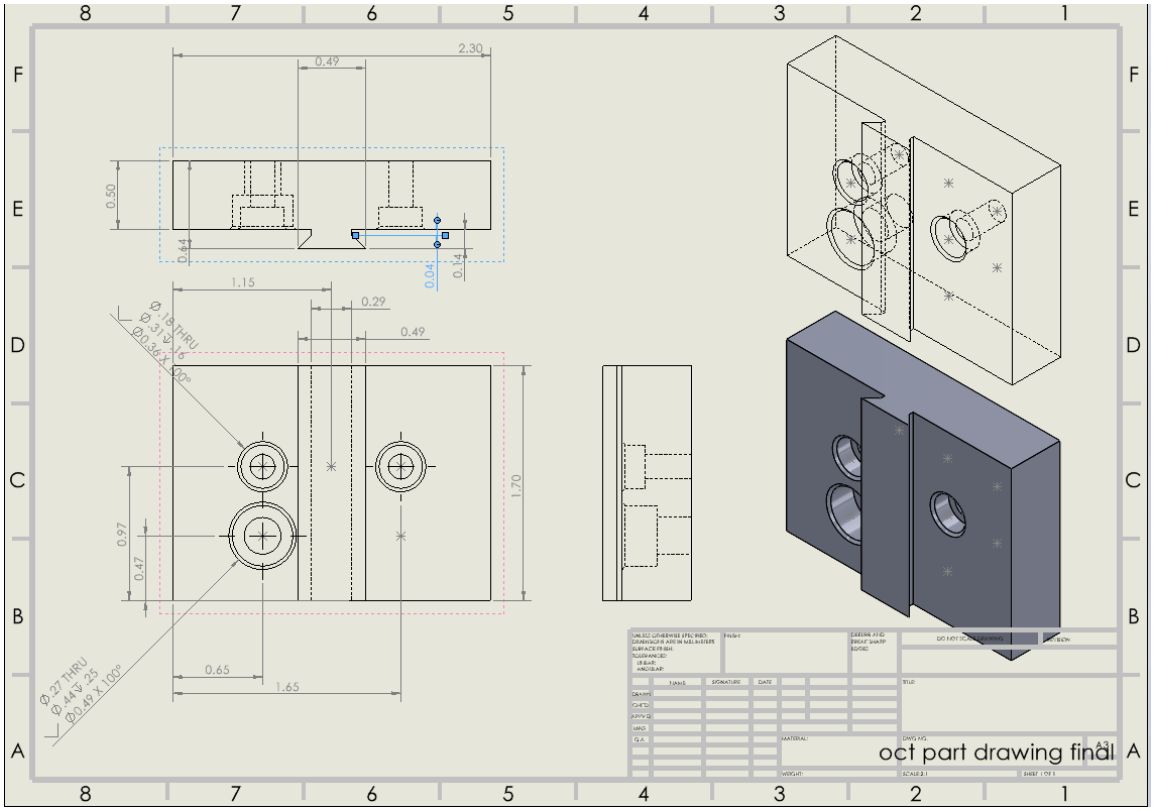

Figure B.5. Engineering Drawing of Connector: The engineering drawing for the connector part between the galvanometer housing and OCT stand is depicted in the above image.

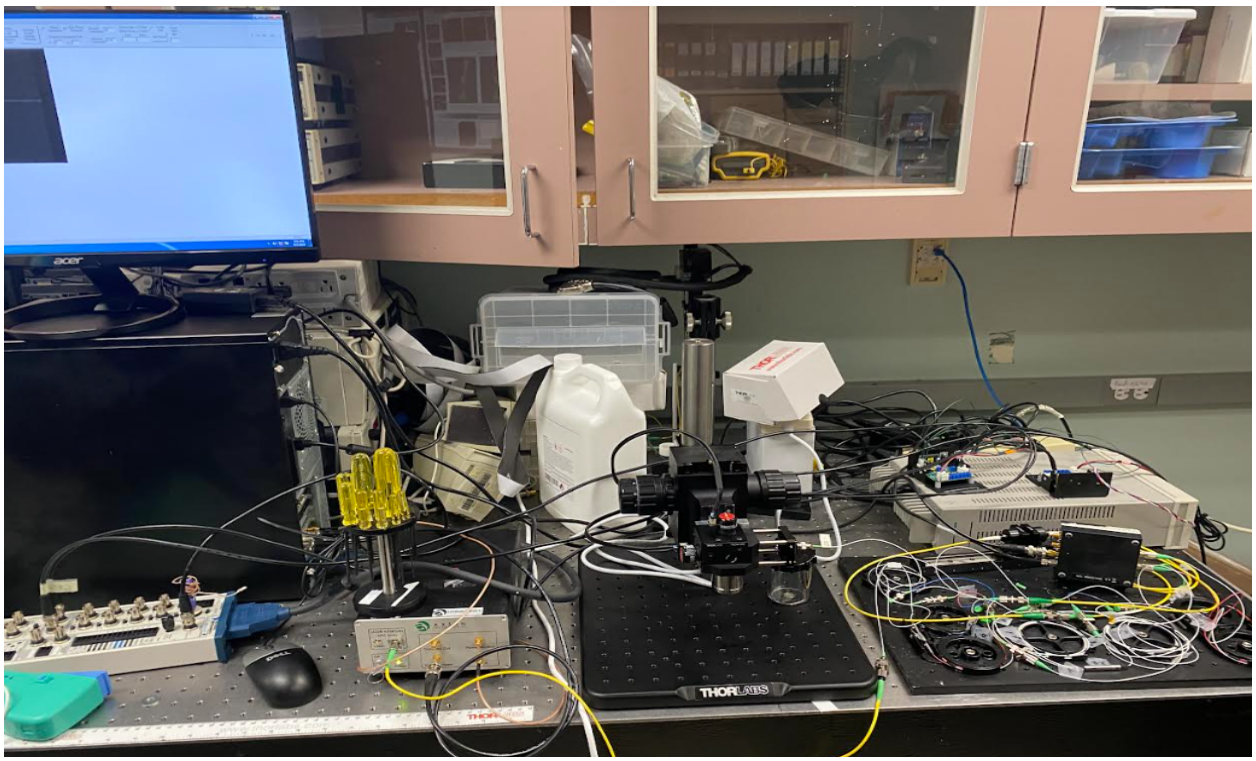

Figure B.6. Assembled SS-OCT System: The above image displays the fully assembled SS-OCT system, featuring all components including the laser, OCT stand, interferometer, computer, and power supply units.

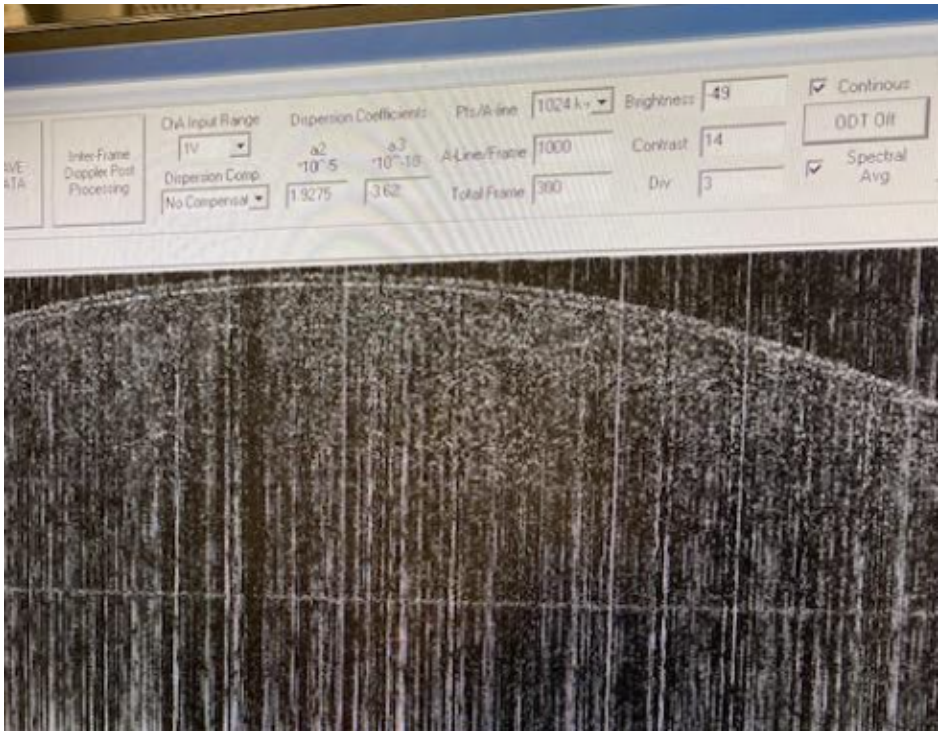

Figure B.7. Sample SS-OCT Image: The provided image showcases an OCT image obtained using the system, with the sample being a globe from a New Zealand white rabbit.